QUANTITATIVE ANALYSIS OF THE EFFECT OF PERFORATION INTERACTION ON SAND PRODUCTION USING THE FINITE ELEMENT METHOD

A Thesis

by

NAOTO ARAKI

Submitted to the Office of Graduate and Professional Studies of
Texas A&M University
in partial fulfillment of the requirements for the degree of

MASTER OF SCIENCE

Chair of Committee,	Nobuo Morita
Committee Members,	Jihoon Kim
	Hiroko Kitajima
Head of Department,	Jeff Spath

August 2018

Major Subject: Petroleum Engineering

ABSTRACT

The study investigates perforation interaction in order to find the optimum perforation design which yields the highest productivity while maintaining mechanical stability.

The study is composed of i) evaluation of flow performance and ii) evaluation of mechanical stability. Both evaluations were performed by using the finite element method with multi-perforation mesh to distinguish the effect of perforation interaction.

The flow evaluation quantitated the productivity for various cases, allowing us to find the most prolific perforation design.

In the stability evaluation, perforation stability was quantitated under various conditions with the effect of perforation interaction. It provides us with a new insight into the effect of shot density on perforation stability.

ACKNOWLEDGEMENTS

I would like to thank my advisor, Dr. Morita, and my committee members, Dr. Kim and Dr. Kitajima, for their guidance and support throughout my academic work.

Thanks also go to my friends and colleagues and the department faculty and staff for making my time at Texas A&M University a great experience. Finally, thanks to my wife and daughter for their encouragement, patience and love.

CONTRIBUTORS AND FUNDING SOURCES

Contributors

This work was supervised by a thesis committee consisting of Dr. Morita [advisor], Dr. Kim [committee member] of the Department of Petroleum Engineering and Dr. Kitajima [committee member] of the Department of Geology and Geophysics at Texas A&M University.

All other work conducted for the thesis was completed by the student independently.

Funding Sources

There are no outside funding contributions to acknowledge related to the research and compilation of this document.

NOMENCLATURE

σ	effective stress
σ_θ	effective tangential stress
σ_v	effective vertical stress
σ_r	effective radial stress
k_x	permeability in x-direction
k_y	permeability in y-direction
k_z	permeability in z-direction
$k_{perf\text{-}damage}$	permeability of perforating damaged zone
$k_{nud\text{-}damage}$	permeability of drilling mud damaged zone
$k_{reservoir}$	permeability of reservoir without damage

TABLE OF CONTENTS

Page

Page

LIST OF FIGURES

Page

LIST OF TABLES

Page

1. INTRODUCTION AND STATEMENT OF PROBLEM

1.1. Sand Production Problem in Oil/Gas Field

When oil and gas are produced from sandstone reservoirs, perforation surface may be failed due to the increase in effective stress. The failed sand particles are carried from perforations into the well by fluid flow. Except for heavy oil production in which sand is intentionally produced to enhance productivity, the produced sand is an unwanted byproduct.

The sand production problem has been a common issue in oil and gas fields. For example, BP estimates 60% of its production comes from sand-prone reservoirs (Liou, 2014). The risk of sand production is unavoidable as long as we produce oil and gas from sandstone or sand reservoir. If sand production occurs, hydrocarbon flow rate should be reduced because sand particles at high velocity are abrasive inducing severe erosion not only at surface facilities but also inside the well. In addition to that, when fluid flow is not high enough, sand will deposit in a well and causing sand-up problems. Even if the sand is transported to surface, sand accumulation in a separator and handling of the produced sand are troublesome.

Several methods are available to mitigate sand problems such as installation of stand-alone sand screen, gravel pack or choking the flow rate. However, these sand control methods reduce not only the production of sand but also reduce production of hydrocarbon as the result of the flow restriction. It is apparent that, although those sand

control methods are widely used and have successfully prevented sand production, doing so is not necessarily the most economic decision. Therefore, whenever sand control is designed, stability of perforations should be also considered to find the economically optimum method to reduce sand problems. The integrated approach is also known as sand management rather than sand control. In order to optimize the sand management strategy, we need to know the perforation pattern and density to reduce sand problems with the highest flow efficiency.

1.2. Mechanism of Sand Production / Estimation of the Onset of Sand Production

Sand production occurs when i) sand face rock is failed and ii) the failed rock is transported into the well.

As in any rock deformation, failure of the sand face is govern by stress condition and strength of the rock. Stresses on the perforation cavity are induced by in-situ stress due to overburden and tectonic stress, pore pressure and hydraulic head of drilling fluid. Although the in-situ stress can be considered as constant, pore pressure and hydraulic head of drilling fluid will be changed during the field life.

In downhole condition, formation rock shows highly ductile behavior. Therefore, failure of the rock is often judged by plastic strain criterion rather than stress criteria as it is more practical to identify the failure.

The type of failure includes shear failure and tensile failure. Tensile stress is exerted on cavity surface when formation fluid is produced. However, as long as the rock is intact (not failed), tensile stress due to the fluid flow is not enough to destroy the

rock in most cases (E. Fjaer, 2008). Tensile failure will occur only when extremely high drawdown is applied or non-darcy flow occurs.

After the failure of sand, the fragment or particle of sand must be transported from cavity surface into the well. The transport process includes (Arii, Morita, Ito, & Takano, 2005);

- Sand particle is dislodged from cavity surface
- Sand particle flows out from perforation section
- Sand bridge or sand arch is destroyed due to high fluid velocity
- Sand particle is lifted from the well to surface

As described above, without sufficient fluid flow, sand production will not occur even though the cavity surface is mechanically failed. Therefore, it is thought that post-failure behavior affects sand production. To quantify the behavior, Arii et al. (2005) performed experiments for various cavity size and grain size, and showed required flow rate to destroy sand bridge/arch and carry the sand. Wang and Sharma (2017) carried out numerical study which simulates the change of cavity geometry caused by rock failure and transport of failed sand. However, post-failure behavior of the cavity is still open to question.

To predict the sand production, critical drawdown diagram is widely used because of its simplicity. As the method is highly simplified, it may provide less insight to depict the severity of sand production and effect of flow performance. On the other hand, when sufficient data is available, semi-analytical model and numerical model can be used. Sand Predictor developed by SINTEF is known as a semi-analytical model

which enables fast analysis based on log data. Most numerical method for 3D problem employs finite element method since it is a powerful method for elasto-plastic problem in a complex geometry.

1.3. Problem Statement

In previous studies including experiment and numerical study, they had focused on the stability of a single perforation. Those observation and finding are important and significant, however, stability of multiple perforations with their interaction has not been well studied so far. In the real field, it is common that a reservoir section in the well has hundreds of perforations. If the number of perforations are increased, the flow efficiency is increased. It also reduces the vertical and tangential stresses, resulting in delay of on-set of sand production. However, if the density is too high, it increases radial stress, causing early on-set of sand production. Higher perforation density in today's practices gives rise to interests of the interaction between closely spaced perforations.

Understanding the interaction between perforations will also give new knowledge to enhance the study on sand production rate. Prediction of sand rate has been a challenge in the industry resulting in less accuracy. It is said that the predictive accuracy of sand rate by the existing model is 0.01 to 100 times of actual sand rate observed in the field (Fuh and Morita (2013)). There are many factors which lower the prediction accuracy of sand rate such as rock heterogeneity, grain size effect, capillary pressure, chemical reaction, irregular cavity geometry etc. The interaction between perforations is also one of the factors. Therefore, proper understanding of the perforation

interaction is necessary not only for the prediction of the onset of sand production but also for sand rate prediction. Thus, in this study, the author focuses on the onset of the sand production by considering perforation interaction.

The objective of the research is not to simply find a solution to avoid sand production. It intends, through understanding of perforation interaction, to provide insights to obtain optimal design which yields sufficient flow performance without problematic sand production. Therefore, a parametric analysis was carried out in this research to show the mechanical stability and flow performance of each perforation configuration.

2. FINITE ELEMENT METHOD IN ELASTO-PLASTIC PROBLEM

2.1. Theory of the Finite Element Method

The concept of the finite element method (FEM) is to divide the body into finite number of elements and obtain an approximate solution by solving the governing equations for the discretized body. FEM has been used in various fields such as aerospace, automotive, hydrodynamics, electronics, medical science and so on (Yacob Fish, 2007).

A set of governing equations and boundary conditions is called strong form of the problem. To derive finite element equations, the strong form of the problem needs to be converted in to integral form which is known as weak form. Strong form is equivalent to weak form.

Weak form can be derived from strong form by introducing weight function and performing integration by part. Weak form is also derived from the principle of minimum potential energy.

In structural analysis, the weak form is known as the principle of virtual work;

$$\int_{\Omega} [\delta \boldsymbol{\epsilon}]^T \boldsymbol{\sigma} d\Omega - \int_{\Omega} [\delta \boldsymbol{u}]^T \boldsymbol{b} d\Omega - \int_{\Gamma} [\delta \boldsymbol{u}]^T \boldsymbol{t} d\Gamma = 0$$

where

$\boldsymbol{\sigma}$: the vector of stresses,

$\boldsymbol{t}$: the vector of boundary tractions

$\delta \boldsymbol{u}$: the vector of virtual displacement

$\delta\boldsymbol{\epsilon}$: the vector of virtual strain

Ω : the domain of interest

Γ_t : the boundary on which boundary tractions are prescribed

It means that variation of internal work is equal to variation of external work for given displacement $\boldsymbol{u}$ and the displacement solution satisfies its governing equation and boundary condition.

2.2 Numerical Simulation

This research utilized in-house geomechanics simulator. The geomechanics simulator is capable of handling a poro-elasto-plastic deformation of material in 3D. Fundamental structure and function of each process are described in Figure 1.

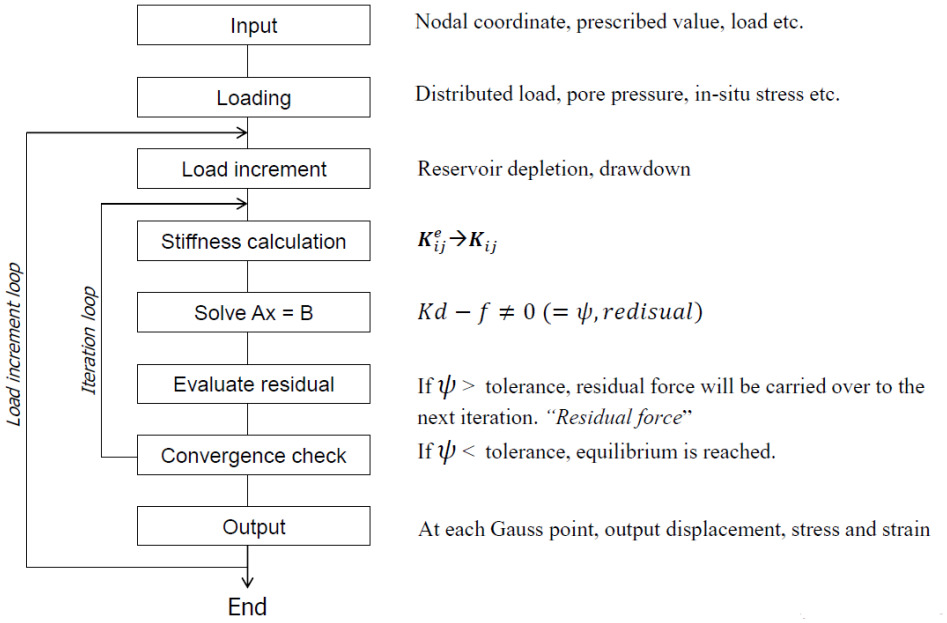

Figure 1 Fundamental Program Structure for Poro-elasto-plastic Model

Since this study investigates perforation interaction in terms of both mechanical stability and fluid flow, flow performance is quantitatively evaluated by in-house flow simulator. In addition, a new mesh generator was developed to create multi-perforation wellbore mesh which includes perforation patterns such as 120°/60° phasing (symmetry), 180°/90° phasing (symmetry), 180°/60° phasing (double spiral) and 90° phasing (single) with 0.5 – 12 SPF (shot per foot). Detail of each perforation configuration is explained in Section 3. Also developed is post-processing program to allow us to visually observe the deformation behavior of the 3D model.

2.3 Failure Criteria

When perforation cavity is about to fail, the material shows highly plastic behavior which makes it difficult to judge the failure based on stress level. Instead of that, critical plastic strain failure criteria is used in this research. Zoback (2007) compared two prediction results of borehole breakout problem, one is predicted by using plastic strain criterion and the other is done by using Mohr-Coulomb failure criterion. They are quite similar indicating the validity of plastic strain criterion.

Figure 2 shows the schematic of plastic strain in 1D (modified from Hinton (1980)).

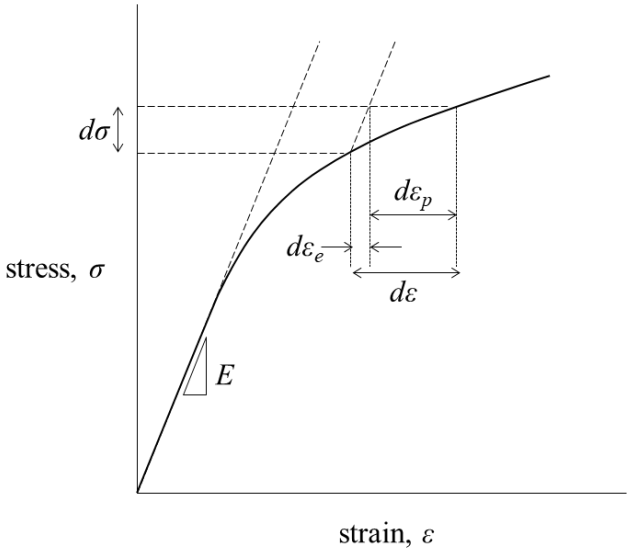

Figure 2 Schematic of Stress – Strain Curve for Elasto-Plastic Material

Accounting for plastic strain in every direction, scalar of plastic strain is calculated from the following equation.

$$\epsilon_p^e = \sqrt{\frac{2}{3}\epsilon_{ij}^p \epsilon_{ij}^p} = \sqrt{\frac{2}{3}\{(\epsilon_z^p)^2 + 2(\epsilon_r^p)^2\}}$$

The obtained effective plastic strain will be compared with critical plastic strain to judge failure. In this study, plastic strain at the end of each tri-axial test is used as critical plastic strain.

3. PALAMETRIC STUDY OF FLOW PERFORMANCE AND MECHANICAL STABILITY

3.1. Introduction

In order to model the wellbore with multiple perforations, an in-house elasto-plastic simulator which is based on the finite element method (FEM) is employed in the research. To achieve the objectives, multi-perforation mesh was newly created and post-processing program was improved to allow better observation of the complicated structure.

The parametric study investigates the flow performance of the perforation and its mechanical stability by changing the parameters, which include perforation phase (angle between adjacent perforations), perforation density (number of perforations in a unit interval), perforation diameter, perforation length, in-situ stress, well inclination, formation strength, permeability, reservoir depletion and so on.

Flow performance is evaluated as productivity ratio which is non-dimensional value and widely used to quantitate the perforation flow performance (Karakas & Tariq, 1991). Mechanical stability of the perforation will be evaluated by comparing the effective plastic strain at each Gauss point (each element has 3^3 Gauss points) with critical plastic strain.

3.2 Mesh

A mesh used in this study is created to model a well with multiple perforations. The model is composed of 5, 7, 9, 11 or 13 planes along wellbore axis with 10 to 14 perforations in total. Longitudinal distance between perforations and perforation phasing are determined so that the mesh becomes symmetrical or near symmetrical about the center perforation in the model. Only the perforation(s) on the middle layer is used for failure evaluation to minimize the effect from top and bottom boundary.

Depending on perforation pattern and shot density, the model has 9,000 to 13,000 elements in total. The elements are 20-node brick element except for the external elements which are infinite elements to account for infinite extent of surrounding rock. For any perforation configuration, elements around perforation have basically the same geometry and dimension to minimize the effect of the difference in mesh.

In this study, we assume that casing is stable and annulus is perfectly cemented. Thus, wellbore and perforation entrance are also considered as stable in the model. From this reason, the model accounts for only a part of perforation which penetrates reservoir rock. The other part which is across casing and cement is not modeled as it does not affect sand production problem. Example of the mesh is shown in Figure 3 and perforation patterns are shown in Figure 4. The model mesh used in this study is visualized by using ParaView (Ahrens (2005)).

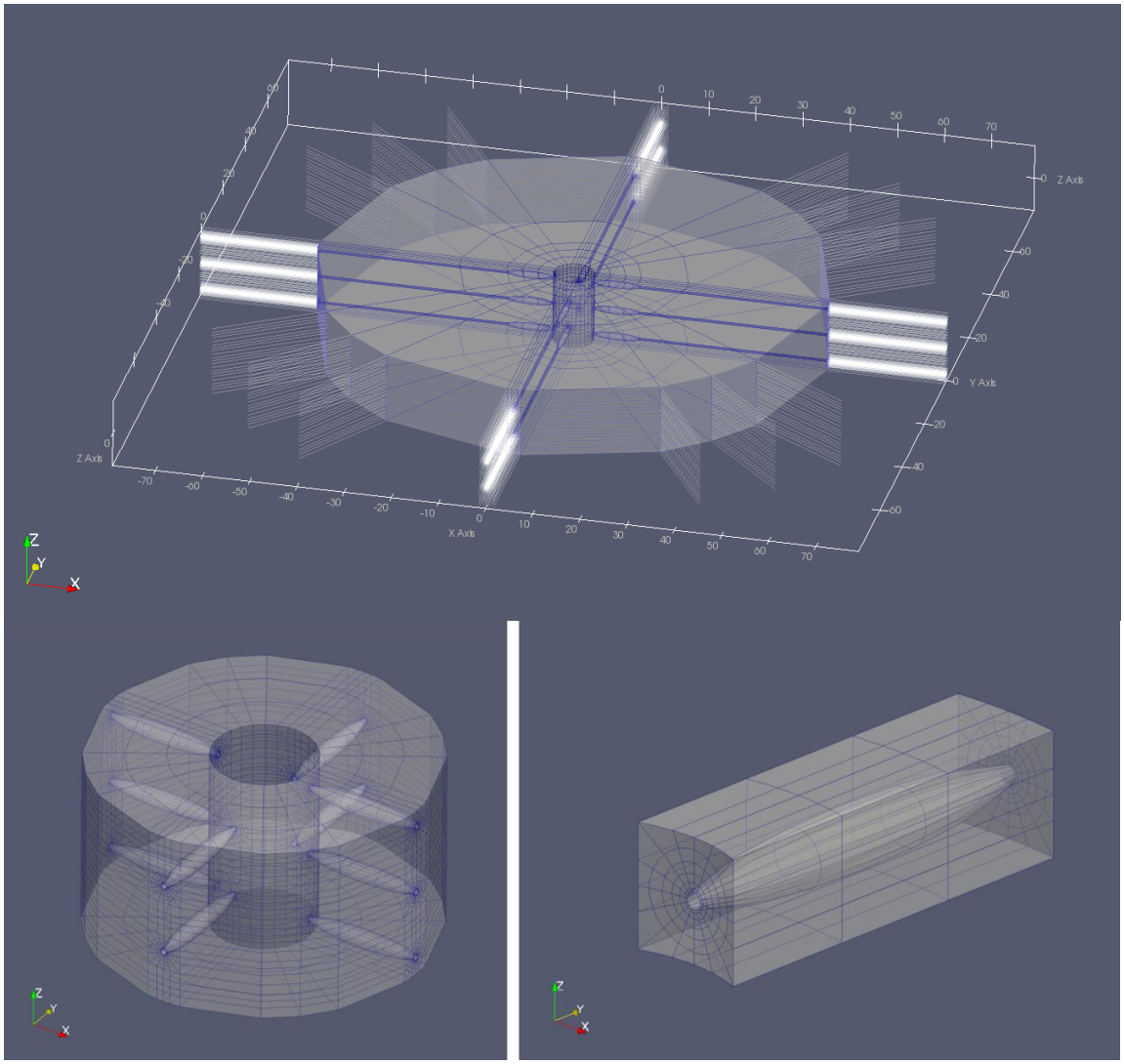

Figure 3 Example of the Mesh for 180°/90° Phasing with SPF 4 (Overall Structure (top), Extracted Mesh around Well and Perforations (bottom left) and Extracted Perforation Mesh (bottom right))

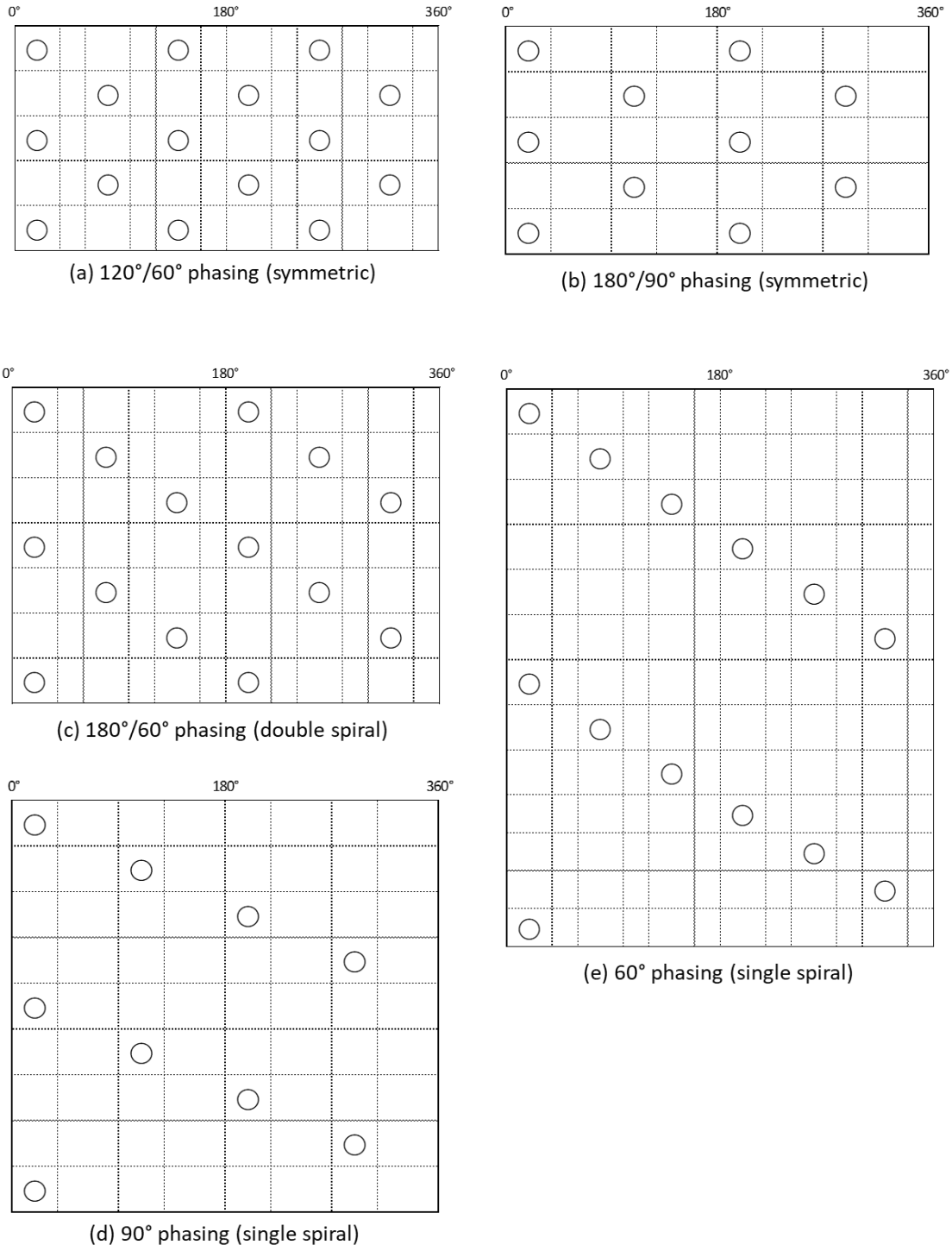

Figure 4 Perforation Pattern (Vertical dimension other than middle layer varies by shot density. A box with a circle correspond to *perforation mesh* shown in Figure 3)

3.3. Evaluation of Flow Performance

3.3.1 Fluid Flow Model

Although each perforation configuration has unique combination of parameters (phasing, shot density, perforation diameter, perforation length etc.), it is necessary to quantitate the flow performance of all the perforation configurations on the same basis. Productivity ratio *J* which is defined as below is used to quantitate flow performance (W.T. Bell, 1995).

$$J = \frac{q_p}{q_{oh}} = \frac{\ln\left(\frac{r_e}{r_w}\right)}{\ln\left(\frac{r_e}{r_w}\right) + s_t}$$

where q_{oh} = flow from ideal open hole (no permeability damage), q_p = flow from perforated system, r_e = drainage radius, r_w = wellbore radius and s_t = total skin.

By using numerical flow simulation, q_p was obtained at steady state regime. The mesh used for flow simulation is basically same as the mesh used in geomechanics simulation (Section 3.4) except for most external elements. In geomechanics model, the external elements are infinite elements to account for infinite extent of rock. On the other hand, in the flow model, the external elements are finite elements in order to set specific drainage radius to obtain steady state solution.

For validation of the numerical flow model, q_{oh} from numerical simulation is compared with analytical solution. The r_e is set to 1320 ft which corresponds to the drainage radius for 40 acre well spacing and r_w is set to 4.25 inch (8.5" hole). Single

phase flow (oil) is assumed with fluid density 0.75 g/cc and viscosity 1.4 cp. As the fluid properties are assumed to be constant with pressure (independent of pressure), pressure boundary conditions are; 0 psi at external boundary and -1kpsi at sand face.

Error check of the flow model was performed as below.

Flow rate for steady state radial flow is;

$$q = \frac{2\pi kh}{\mu}\left(r\frac{\partial p}{\partial r} \right)$$

The general solution of the radial steady state solution is given by

$$dp = \frac{q\mu}{2\pi kh}\frac{dr}{r}$$

or

$$\int_{r_w}^{r_e} dp = \frac{q\mu}{2\pi kh}\int_{r_w}^{r_e}\frac{dr}{r}$$

$$p_e - p_w = \frac{q\mu}{2\pi kh}\ln\left(\frac{r_e}{r_w}\right)$$

Using the Darcy's unit, we have for $r_e = 1320\,ft$

$$p_e - p_w = 1000\,psi = 68.046atm$$

$$k = 0.1dacy$$

$$\mu = 1.4cp$$

H = 3 × 7 inches = 53.34cm

$$\ln\left(\frac{r}{r_w}\right) = \ln\left(\frac{1320}{0.3541666}\right) = 8.223374$$

$$q = \frac{2\pi kh}{\mu}\frac{p_e - p_w}{\ln(r_e / r_w)} = \frac{2\pi \times 0.1 \times 53.34}{1.4}\frac{68.046}{8.223374} = 198.08765 cc / \sec$$

The numerical model for a borehole without any damage gives 199.46cc/sec for 1320 × 12 inch external boundary. It is 0.69 % higher (the error 0.69%).

3.3.2 Result and Discussion of Flow Performance

3.3.2.1 General

Effect of perforation parameters on productivity is described in this section. The parameters studied include; perforation pattern, shot density, perforation length and diameter, permeability damage by drilling mud and perforating, and enlarged cavity induced by sand production. Result of the flow evaluation is summarized in Table 1.

Note that the following conditions are assumed unless otherwise stated.

- perforation diameter 1.0” at the middle of the perforation tunnel
- perforation entrance diameter 0.4”
- perforation length 10.0”
- well inclination 0° (vertical well)
- no permeability damage

The other parameters are same as in section 3.3.1.

Table 1 Summary of Flow Performance

Phasing		sym / spiral	symmetry	symmetry	symmetry	symmetry	symmetry	symmetry	double spiral	double spiral	double spiral	double spiral	single spiral	single spiral	single spiral	single spiral
		°	120/60	120/60	120/60	180/90	180/90	180/90	180/60	180/60	180/60	180/60	90	90	90	90
Shot Density		SPF	12	6	3	8	4	2	8	6	4	2	4	3	2	1
Perofation Entrance Diameter		in	0.2	0.2	0.2	0.2	0.2	0.2	0.2	0.2	0.2	0.2	0.2	0.2	0.2	0.2
Perofatino Diameter at Middle		in	0.75	0.75	0.75	0.75	0.75	0.75	0.75	0.75	0.75	0.75	0.75	0.75	0.75	0.75
Perofation Length		in	10	10	10	10	10	10	10	10	10	10	10	10	10	10
Productivity Ratio		-	1.121	1.096	1.048	1.100	1.067	0.997	1.106	1.090	1.057	0.969	1.059	1.024	0.964	0.825
Reservoir Permeability		mD	100	100	100	100	100	100	100	100	100	100	100	100	100	100
Perforating Damage	Permeability	mD	-	-	-	-	-	-	-	-	-	-	-	-	-	-
	Thickness	in	-	-	-	-	-	-	-	-	-	-	-	-	-	-
Mud Damage	Permeability	mD	-	-	-	-	-	-	-	-	-	-	-	-	-	-
	Thickness	in	-	-	-	-	-	-	-	-	-	-	-	-	-	-

Phasing		sym / spiral	symmetry	symmetry	symmetry	symmetry	symmetry	symmetry	symmetry	symmetry	symmetry	symmetry	symmetry	symmetry	symmetry	double spiral	double spiral	double spiral	double spiral	single spiral	single spiral	single spiral	single spiral
		°	120/60	120/60	120/60	120/60	180/90	180/90	180/90	180/90	180/90	180/90	180/90	180/90	180/90	180/60	180/60	180/60	180/60	90	90	90	90
Shot Density		SPF	12	6	4	3	8	4	2	8	4	2	8	4	2	8	6	4	2	4	3	2	1
Perofation Entrance Diameter		in	0.2	0.2	0.2	0.2	0.2	0.2	0.2	0.2	0.2	0.2	0.2	0.2	0.2	0.2	0.2	0.2	0.2	0.2	0.2	0.2	0.2
Perofatino Diameter at Middle		in	0.5	0.5	0.5	0.5	0.5	0.5	0.5	0.5	0.5	0.5	0.5	0.5	0.5	0.5	0.5	0.5	0.5	0.5	0.5	0.5	0.5
Perofation Length		in	10	10	10	10	10	10	10	10	10	10	10	10	10	10	10	10	10	10	10	10	10
Productivity Ratio		-	1.115	1.086	1.057	1.031	1.092	1.052	0.975	1.087	1.044	0.961	1.061	1.002	0.893	1.097	1.078	1.041	0.942	1.043	1.006	0.940	0.792
Reservoir Permeability		mD	100	100	100	100	100	100	100	100	100	100	100	100	100	100	100	100	100	101	102	103	104
Perforating Damage	Permeability	mD	-	-	-	-	-	-	-	20	20	20	20	20	20	-	-	-	-	-	-	-	-
	Thickness	in	-	-	-	-	-	-	-	0.082	0.082	0.082	0.262	0.262	0.262	-	-	-	-	-	-	-	-
Mud Damage	Permeability	mD	-	-	-	-	-	-	-	-	-	-	-	-	-	-	-	-	-	-	-	-	-
	Thickness	in	-	-	-	-	-	-	-	-	-	-	-	-	-	-	-	-	-	-	-	-	-

Phasing		sym / spiral	symmetry	symmetry	symmetry	symmetry	symmetry	symmetry	symmetry	symmetry	symmetry	symmetry	symmetry	symmetry	symmetry	symmetry	symmetry	symmetry	symmetry	symmetry	symmetry	symmetry	symmetry
		°	180/90	180/90	180/90	180/90	180/90	180/90	180/90	180/90	180/90	180/90	180/90	180/90	180/90	180/90	180/90	180/90	180/90	180/90	180/90	180/90	180/90
Shot Density		SPF	8	4	2	4	4	4	4	4	4	4	4	4	4	4	4	4	4	4	4	4	4
Perofation Entrance Diameter		in	0.2	0.2	0.2	0.2	0.2	0.2	0.2	0.2	0.2	0.2	0.2	0.2	0.2	0.2	0.2	0.2	0.2	0.2	0.2	0.2	0.2
Perofatino Diameter at Middle		in	0.5	0.5	0.5	0.5	0.5	0.5	0.5	0.5	0.5	0.5	0.5	0.5	0.5	0.5	0.5	0.5	0.5	0.5	0.5	0.5	0.5
Perofation Length		in	15	15	15	10	10	10	10	10	10	10	10	10	10	10	10	10	10	10	10	10	10
Productivity Ratio		-	1.143	1.111	1.046	1.052	1.041	1.013	0.953	1.044	1.032	1.004	0.947	1.002	0.991	0.968	0.929	0.984	0.975	0.954	0.921		
Reservoir Permeability		mD	100	100	100	100	100	100	100	100	100	100	100	100	100	100	100	100	100	100	100		
Perforating Damage	Permeability	mD	-	-	-	-	-	-	-	20	20	20	20	20	20	20	20	20	20	20	20		
	Thickness	in	-	-	-	-	-	-	-	0.028	0.028	0.028	0.028	0.262	0.262	0.262	0.262	0.412	0.412	0.412	0.412		
Mud Damage	Permeability	mD	-	-	-	-	40	40	40	-	40	40	40	-	40	40	40	-	40	40	40		
	Thickness	in	-	-	-	0	3.25	6.5	9.75	0	3.25	6.5	9.75	0	3.25	6.5	9.75	0	3.25	6.5	9.75		

Table 2 Summary of Flow Performance (Effect of Vertical Permeability)

Phasing		sym / spiral	symmetry	symmetry	single spiral	double spiral
		°	180/90	120/60	90	180/60
Shot Density		SPF	4	4	4	4
Perofation Entrance Diameter		in	0.2	0.2	0.2	0.2
Perofatino Diameter at Middle		in	0.5	0.5	0.5	0.5
Perofation Length		in	10	10	10	10
Perforating Damage	Permeability	mD	-	-	-	-
	Thickness	in	-	-	-	-
Mud Damage	Permeability	mD	-	-	-	-
	Thickness	in	-	-	-	-
Productivity Ratio						
Permeability $k_x, k_y, k_z = 100,100,1$			0.805	0.794	0.766	0.760
Permeability $k_x, k_y, k_z = 100,100,10$			0.945	0.952	0.918	0.916
Permeability $k_x, k_y, k_z = 100,100,100$			1.052	1.057	1.043	1.041

3.3.2.2. Perforation Pattern and Shot Density

Figure 5 shows productivity ratio versus shot density for 120°/60° phasing and 180°/90° phasing pattern. Both patterns yield very similar upward-sloping curves. Productivity ratio greater than 1 is obtained with shot density > 3.

Although 180°/90° phasing pattern has only two perforations in a horizontal plane, its drainage is as efficient as 120°/60° phasing as shown in Figure 6. Vertical drainage is also good in this example since isotropic permeability is assumed in this case (Figure 7).

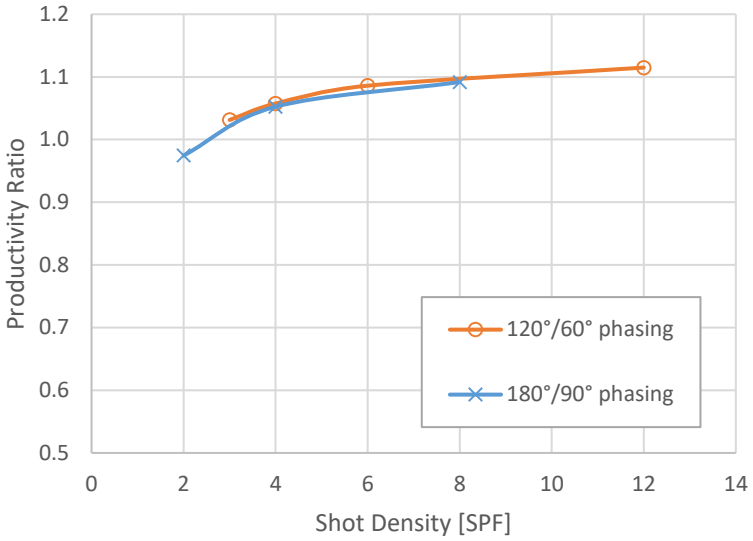

Figure 5 Effect of Perforation Pattern and Shot Density (symmetric pattern; 120°/60° phasing and 180°/90° phasing)

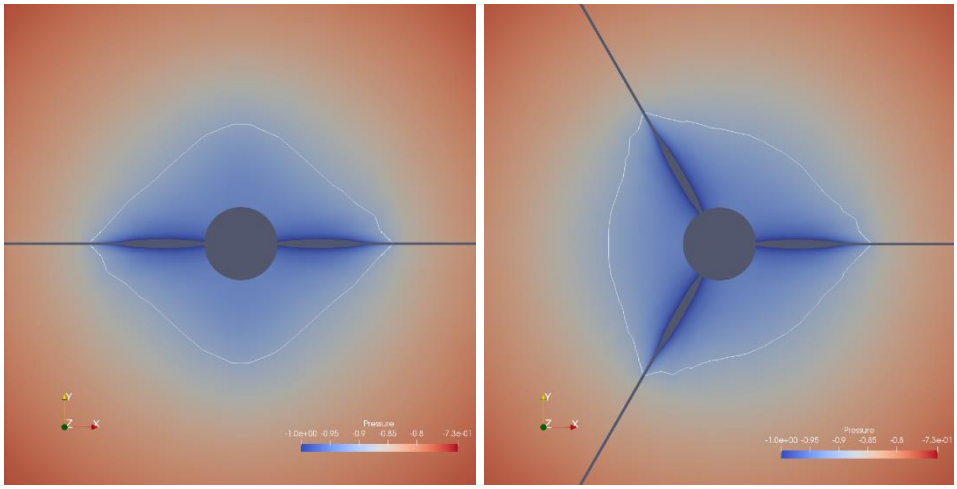

Figure 6 Horizontal Pressure Distribution around Perforations (left; 180°/90° phasing, right; 120°/60° phasing)

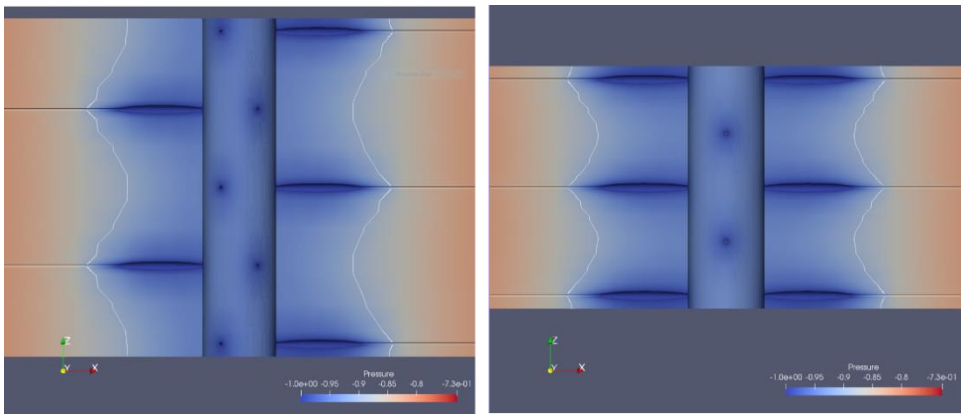

Figure 7 Vertical Pressure Distribution around Perforations (left; 180°/90° phasing, right; 120°/60° phasing)

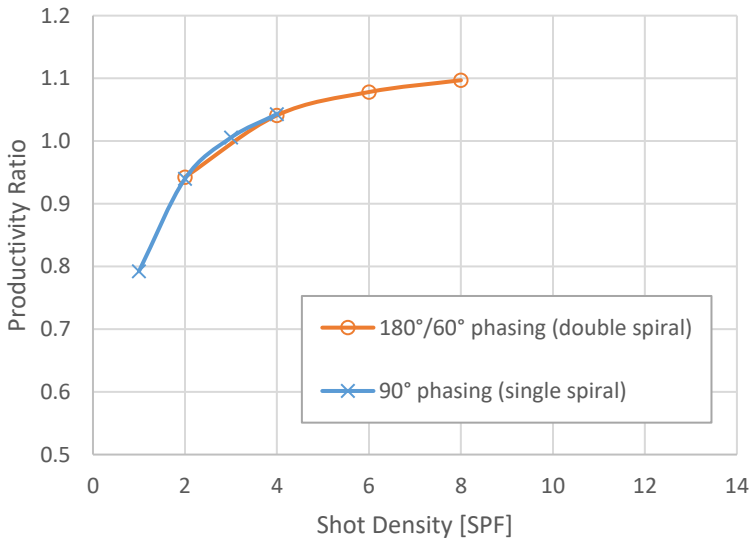

Figure 8 Effect of Perforation Pattern and Shot Density (180°/60° double spiral and 90° single spiral)

Figure 8 shows productivity ratio versus shot density for 180°/60° phasing (double spiral) and 90° phasing (single spiral) pattern. Productivity ratio greater than 1 is obtained with shot density > 3 in either case.

In general, the effect of perforation pattern is more significant with smaller shot density (Figure 9 (a)) than with larger shot density (Figure 9 (b)). For example, with SPF 2, 180°/90° phasing shows the highest productivity ratio. The reason is that the perforations are well-distributed both longitudinally and laterally in 180°/90° phasing SPF 2 as shown in Figure 10. In this case, in which wellbore diameter 8.5" is assumed, the distances between closest perforations are almost the same (see equilateral triangle in Figure 10). On the other hand, at larger shot density, perforations are much closer in any perforation pattern and thus yield almost the same productivity. In other words, perforation pattern could be a bottleneck at small shot density.

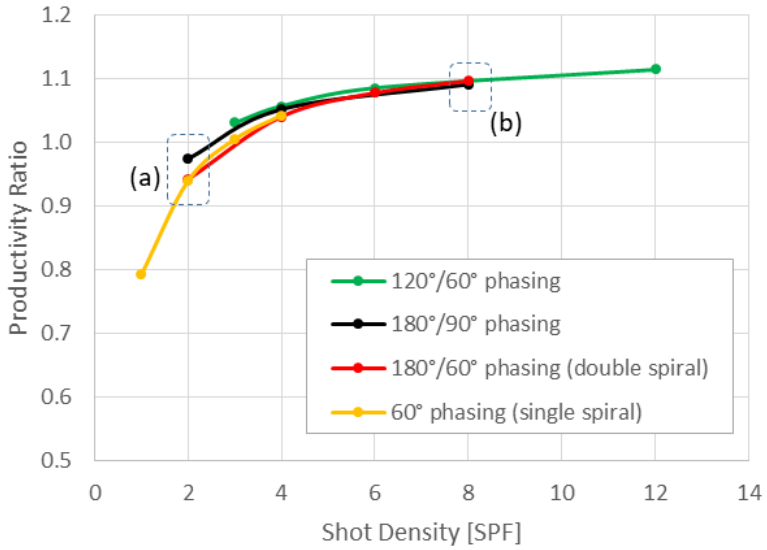

Figure 9 Effect of Perforation Pattern and Shot Density (120°/60° phasing, 180°/90° phasing, 180°/60° double spiral and 60° single spiral)

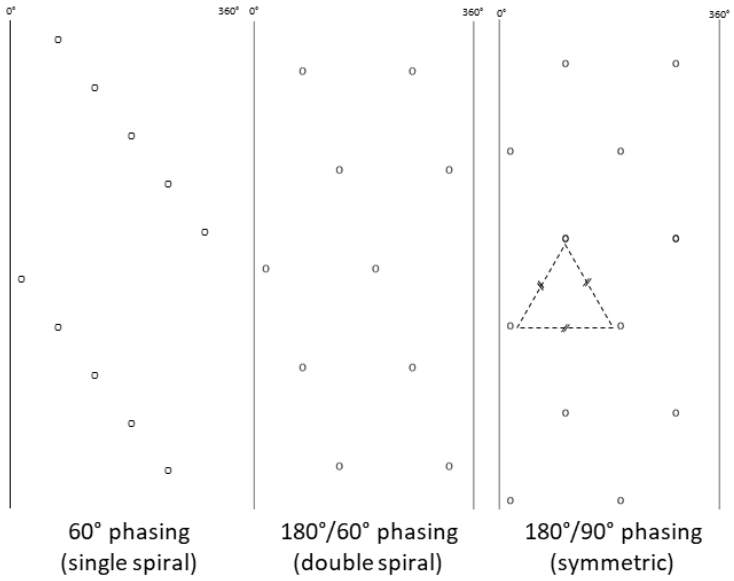

Figure 10 Distribution of Perforations (Width of each diagram corresponds to 0°-360°. Wellbore diameter is 8.5".)

3.3.2.3. Vertical Permeability

In order to see the effect of anisotropic permeability, productivity ratio was calculated for each perforation pattern by changing vertical permeability k_z. Figure 11 shows productivity ratio of each perforation pattern as a function of vertical permeability. Shot density is SPF 4 for all case. As shown in the figure, perforation pattern has small effect on productivity if k_z is large. However, if k_z is small, productivity depends on perforation pattern.

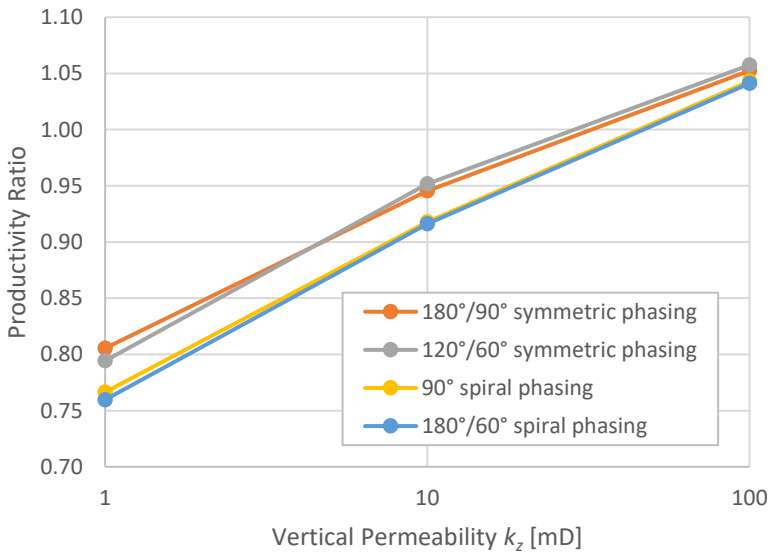

Figure 11 Effect of Vertical Permeability (Shot density is SPF 4)

3.3.2.4 Perforation Length

Only the length is varied with the same perforation diameter. Productivity ratio was increased with increasing perforation length as expected (Figure 12). As will be mentioned later section, longer perforation is more stable if perforation diameter is same and the size effect is ignored. Therefore, longer perforations are better than shorter ones in terms of flow performance and mechanical stability.

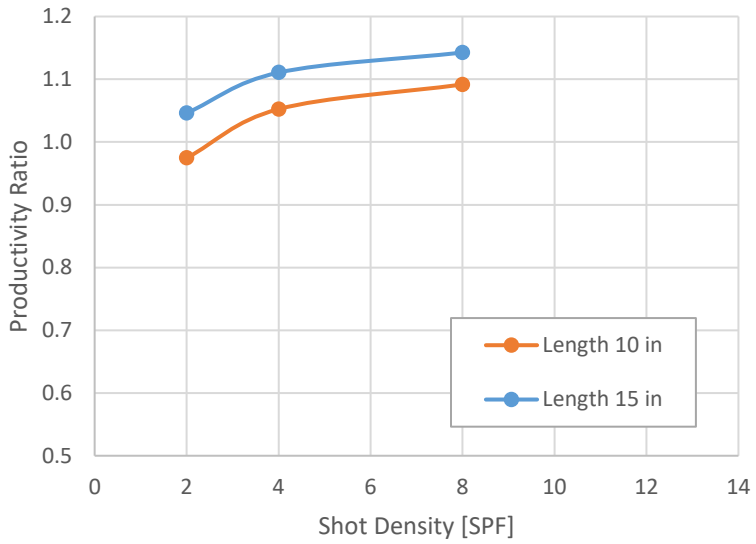

Figure 12 Effect of Perforation Length

3.3.2.5 Perforation Diameter

Figure 13 shows the comparison of productivity ratio for different perforation diameters. The productivity ratio is higher in larger diameter as expected, however, the difference is quite small. The result is consistent with the previous work which says perforation diameter would have minimal effect on well productivity (Karakas and Tariq, 1991).

Although the difference in flow performance is small in the model, actual field would show larger effect because perforation debris and/or failed sand would tend to plug the smaller perforation tunnel.

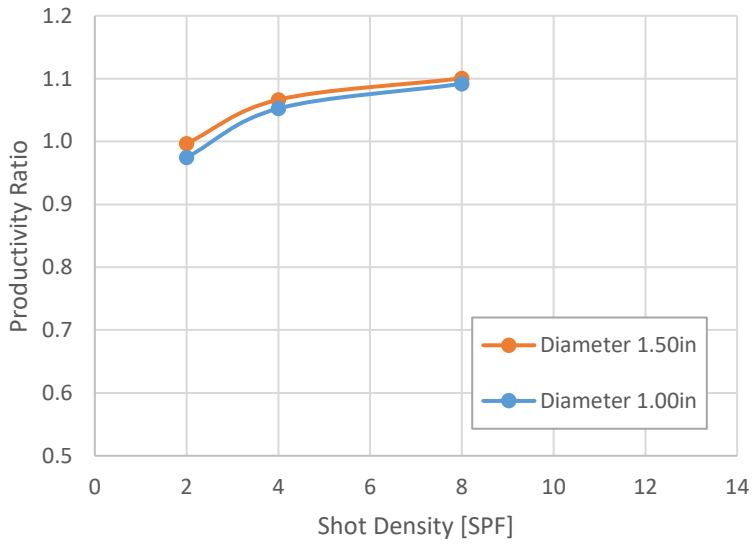

Figure 13 Effect of Perforation Diameter

3.3.2.6 Mud Damage and Perforation Damage

Permeability damage is caused by drilling mud invasion and perforating (Figure 14). Permeability damage occurs on wellbore surface when openhole is filled with drilling mud. In this study, $k_{mud\text{-}damage} / k_{reservoir}$ is set to 0.4 with varying thickness 3.25", 6.50" and 9.75". Perforating damage occurs when shaped-charge penetrates into rock. The rock around perforation tunnel is punched and compacted resulting in lower porosity and permeability. The perforating damage zone is also called crushed zone. Perforation damage is assumed $k_{perf\text{-}damage} / k_{reservoir} = 0.2$ in this study.

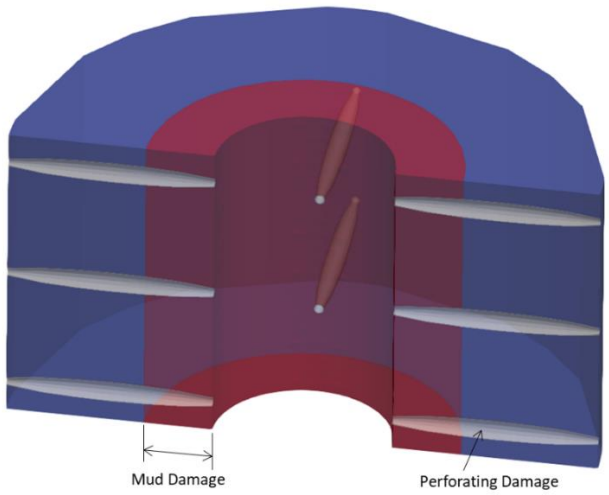

Figure 14 Schematic of Permeability Damage

Effect of perforating damage is shown in Figure 15**.** Reduction in productivity ration due to perforating damage is larger in smaller shot density. The reason is that flow

rate per perforation is higher in smaller shot density resulting in larger impact from perforating damage.

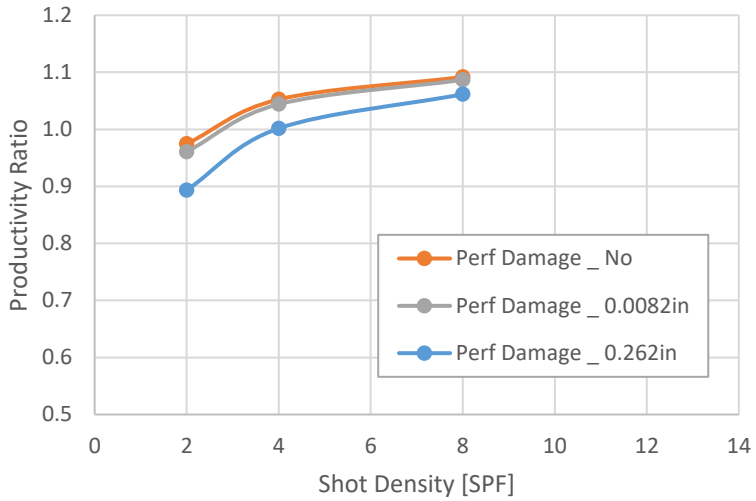

Figure 15 Effect of Perforating Damage

Figure 16 plots productivity ratio as a function of thickness of mud invasion and perforating damage depth. Although the productivity is quantitated under a certain assumption, reduced permeability and damaged zone thickness of drilling mud damage and perforating damage are usually difficult to determine. Therefore, it is practical to check the sensitivity of the parameter as demonstrated in Figure 15 and Figure 16.

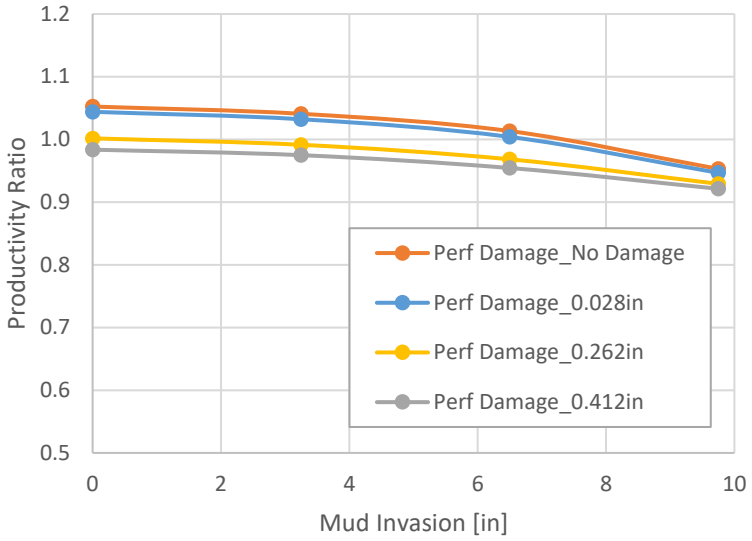

Figure 16 Productivity Ratio as a Function of Thickness of Mud Invasion and Perforating Damage Depth (180°/90° phasing, SPF 4)

3.3.2.7 Effect of Sand Production

In this section, the effect of sand production is evaluated by considering the combined effect of cavity diameter and perforating damage. We assume;

- diameter of perforation is changed from 1.0” to 1.5” as a result of sand production
- sand production (failure of cavity wall) progresses uniformly in a concentric fashion
- perforating damaged zone is removed as a result of sand production

The assumption is within a reasonable range because;

- In a laboratory work done by Papamichos et al. (2008), uniform (concentric) failure was observed under a certain condition
- During that process, the diameter of perforation tunnel was almost doubled after sand production.

The result is shown in Figure 17. The red line is productivity ratio before sand production (ID 1.0” with perforating damage) and the blue line is productivity ratio after sand production (ID 1.5” without perforating damage). As shown in the figure, productivity is increased by sand production. In a real field, more improvement in productivity may be observed because larger diameter would promotes the transport of settled debris.

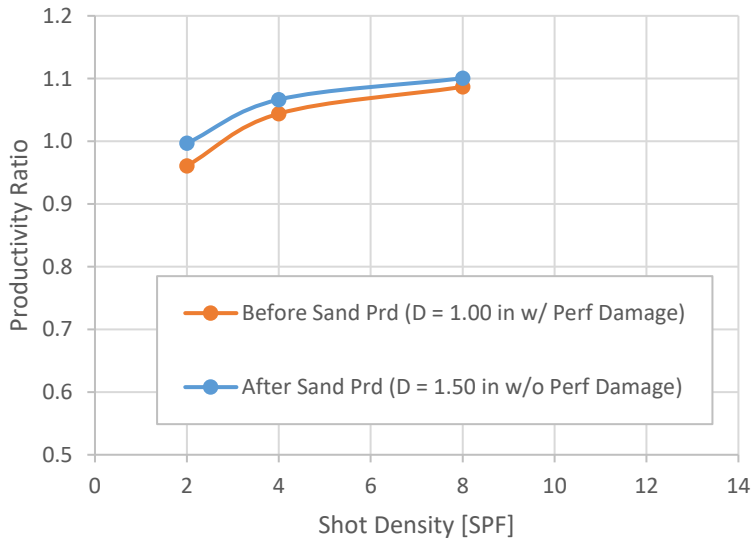

Figure 17 Effect of Sand Production

3.3.3 Summary of Flow Performance Evaluation

- The result of numerical simulation showed that higher shot density yields higher productivity.
- If shot density is low and/ or vertical permeability is low, perforation pattern could be a bottleneck.
- Sand production may enhance productivity by enlarging the perforation tunnel and removing damaged wall.

3.4 Evaluation of Perforation Stability

3.4.1 Geomechanics Model

3.4.1.1 Mesh and Property

The mesh used in the geomechanics model is the same as the mesh used in flow model except for external elements. In the geomechanics model, the most external elements are infinite element in order to account for infinite extent of reservoir rock but finite elements are used in the flow model. Top and bottom of the model are free in x and y direction and fixed in z direction. Internal surface of the well bore are fixed in every direction assuming perfect and rigid cementing. External boundary is fixed at infinite distance from the well.

In order to contribute perforation design, sufficient and necessary parameters were chosen and ranged to quantify the impact on mechanical stability. The parameters

include; perforation phasing, shot density, perforation diameter, perforation length, in-situ stress, depletion and well inclination.

Assumptions in this study are:

- Formation is assumed to be homogeneous.
- Stress strain relation is non-linear based on the Drucker-Prager yield criterion. The hardening is based on plastic-strain-hardening. The constitutive relation is fit to real rocks with 4-8 triaxial tests.

  Note: Constitutive relations based on the Drucker-Prager yield criterion with plastic-strain-hardening fit well to the medium to hard sandstones. Stress-strain curve of the rock is shown in Figure 18. (Young's modulus is 1.84×10^6 psi and Poison's ratio is 0.2625.)
- Maximum plastic strain theorem is used as the failure criteria. Onset of sand production occurs if some area of perforation cavity surface exceeds the failure plastic strain. Note that only the critical plastic strain theory can be used for predicting the failure of highly non-linear sandstone. Critical plastic strain is obtained from plastic strain at the failure which corresponds to the end of triaxial test.
- Perforation cavities are ellipsoidal after perforation. (Figure 3)
- The size effect of rock strength is not considered. Only the effect of stress and flow force on cavity stability are analyzed.

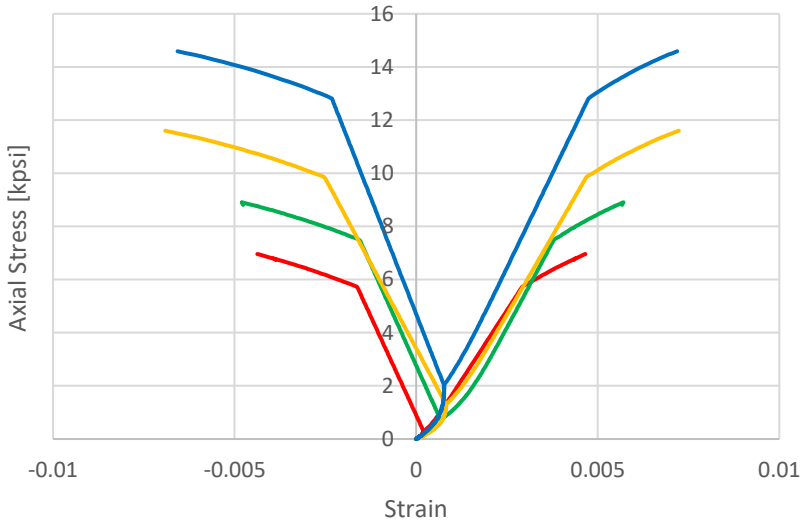

Figure 18 Stress-strain Curve (Data-fitted)

3.4.1.2 Loading Procedure

First, in-situ stress and overbalance (by drilling mud) is gradually applied with the ratio of $\sigma_x : \sigma_y : \sigma_z$ = -0.5 : -0.5 : -1.0 (isotropic stress). Second, the overbalance is released. After releasing the overbalance, the state is equivalent to a stress condition of reservoir which is about to start production. Third, depletion is applied up to a desired level with the ratio of $\sigma_x : \sigma_y : \sigma_z$ = -0.4 : -0.4 : -1.0 (isotropic). As the reservoir is depleted, stresses on perforations are gradually increased and finally reaches its failure condition.

According to E. Fjaer (2008), fluid flow force by drawdown across perforation wall is not high enough to destroy the intact rock. (The force may high enough to remove unconsolidated rock or failed rock and to transport it into the well.) The fact that

the intact rock is not failed under such condition was confirmed by our model by applying drawdown to the rock (same rock as used in this research) after some depletion. Therefore, drawdown is not applied in this study. Perforation failure is evaluated by applying reservoir depletion.

In this study, the loading is based on the following assumption.

- Depth 15,000 ft
- Overburden stress gradient 0.9 psi/ft
- Initial reservoir pressure 10,000 psi
- In-situ vertical effective stress 6,000 psi (= 0.9 psi/ft × 15,000 ft – 10,000 psi)

The ratio of in-situ stress is $\sigma_x : \sigma_y : \sigma_z = -0.5 : -0.5 : -1.0$ unless otherwise stated.
The ratio of stress increment during depletion is $\sigma_x : \sigma_y : \sigma_z = -0.4 : -0.4 : -1.0$ for all cases.

3.4.1.3 Judgement of Failure

As mentioned in 2.3, critical plastic strain failure criteria is used in this study. For every load increment step described above, plastic strain at all Gauss points is evaluated. Once any Gauss point has plastic strain greater than the critical value, the Gauss point is *failed*. As mentioned in Section 1.2, failure of cavity wall does not necessarily mean sand production, however, i) the failure of cavity corresponds to the earliest possible sand production or ii) the failure exactly corresponds to the onset of sand production if there is sufficient fluid flow.

3.4.2 Results of Perforation Stability Evaluation

3.4.2.1 General

Note that the following conditions are assumed unless otherwise stated.

- perforation diameter 1.0” at the middle of the perforation tunnel
- perforation entrance diameter 0.4”
- perforation length 10.0”
- well inclination 0° (vertical well)

Table 3 - Table 7 summarize the perforation configuration, loading condition and depletion at which the perforation starts to fail. Initial in-situ stresses are; σ = -6,000 psi, σx = -3,000 psi and σy = -3,000 psi

Table 3 Summary of Perforation Stability (120°/60° symmetric phasing)

Phasing [°]	120/60	120/60	120/60
Shot Density [SPF]	12	6	3
Depletion [psi]	-3500	-3000	-3060
Perforation Entrance Diameter [in]	0.2	0.2	0.2
Perforation Diameter at Middle [in]	0.75	0.75	0.75
Perforation Length [in]	10	10	10

Phasing [°]	120/60	120/60	120/60
Shot Density [SPF]	12	6	3
Depletion [psi]	-3200	-3025	-3125
Perforation Entrance Diameter [in]	0.2	0.2	0.2
Perforation Diameter at Middle [in]	0.5	0.5	0.5
Perforation Length [in]	10	10	10

Table 4 Summary of Perforation Stability (180°/90° symmetric phasing)

Phasing [°]	180/90	180/90	180/90
Shot Density [SPF]	8	4	2
Depletion [psi]	-3600	-3000	-3040
Perforation Entrance Diameter [in]	0.2	0.2	0.2
Perforation Diameter at Middle [in]	0.75	0.75	0.75
Perforation Length [in]	10	10	10

Phasing [°]	180/90	180/90	180/90
Shot Density [SPF]	8	4	2
Depletion [psi]	-3300	-2900	-3080
Perforation Entrance Diameter [in]	0.2	0.2	0.2
Perforation Diameter at Middle [in]	0.5	0.5	0.5
Perforation Length [in]	10	10	10

Phasing [°]	180/90	180/90	180/90
Shot Density [SPF]	8	4	2
Depletion [psi]	-3500	-3300	-3400
Perforation Entrance Diameter [in]	0.2	0.2	0.2
Perforation Diameter at Middle [in]	0.5	0.5	0.5
Perforation Length [in]	15	15	15

Phasing [°]	180/90	180/90	180/90
Shot Density [SPF]	8	4	2
Depletion [psi]	-2700	-2450	-2350
Perforation Entrance Diameter [in]	0.2	0.2	0.2
Perforation Diameter at Middle [in]	0.5	0.5	0.5
Perforation Length [in]	10	10	10
σx	-300	-300	-300
σy	-300	-300	-300
σz	-1000	-1000	-1000

Table 4 Continued

Phasing [°]	180/90	180/90	180/90
Shot Density [SPF]	8	4	2
Depletion [psi]	-4550	-4100	-4200
Perforation Entrance Diameter [in]	0.2	0.2	0.2
Perforation Diameter at Middle [in]	0.5	0.5	0.5
Perforation Length [in]	10	10	10
σx	-700	-700	-700
σy	-700	-700	-700
σz	-1000	-1000	-1000

Table 5 Summary of Perforation Stability (180°/60° double spiral phasing)

Phasing [°]	180/60	180/60	180/60	180/60
Shot Density [SPF]	8	6	4	2
Depletion [psi]	-3200	-2900	-2800	-2980
Perforation Entrance Diameter [in]	0.2	0.2	0.2	0.2
Perforation Diameter at Middle [in]	0.75	0.75	0.75	0.75
Perforation Length [in]	10	10	10	10

Phasing [°]	180/60	180/60	180/60
Shot Density [SPF]	8	6	4
Depletion [psi]	-3120	-2960	-3200
Perforation Entrance Diameter [in]	0.2	0.2	0.2
Perforation Diameter at Middle [in]	0.5	0.5	0.5
Perforation Length [in]	10	10	10

Table 6 Summary of Perforation Stability (90° single spiral phasing)

Phasing [°]	90	90	90	90
Shot Density [SPF]	4	3	2	1
Depletion [psi]	-3000	-2900	-2800	-3000
Perforation Entrance Diameter [in]	0.2	0.2	0.2	0.2
Perforation Diameter at Middle [in]	0.75	0.75	0.75	0.75
Perforation Length [in]	10	10	10	10

Phasing [°]	90	90	90	90	90
Shot Density [SPF]	4	3	2	1	0.5
Depletion [psi]	-2980	-3200	-3200	-3100	-3300
Perforation Entrance Diameter [in]	0.2	0.2	0.2	0.2	0.2
Perforation Diameter at Middle [in]	0.5	0.5	0.5	0.5	0.5
Perforation Length [in]	10	10	10	10	10

Phasing [°]	90	90	90	90
Shot Density [SPF]	4	3	2	1
Depletion [psi]	-3100	-2900	-2900	-3000
Perforation Entrance Diameter [in]	0.2	0.2	0.2	0.2
Perforation Diameter at Middle [in]	0.625	0.625	0.625	0.625
Perforation Length [in]	10	10	10	10

Phasing [°]	90	90	90	90
Shot Density [SPF]	4	3	2	1
Depletion [psi]	-3400	-3200	-3100	-3100
Perforation Entrance Diameter [in]	0.2	0.2	0.2	0.2
Perforation Diameter at Middle [in]	0.5	0.5	0.5	0.5
Perforation Length [in]	15	15	15	15

Phasing [°]	90	90	90	90
Shot Density [SPF]	4	3	2	1
Depletion [psi]	-2900	-2940	-2900	-3040
Perforation Entrance Diameter [in]	0.2	0.2	0.2	0.2
Perforation Diameter at Middle [in]	0.5	0.5	0.5	0.5
Perforation Length [in]	12.5	12.5	12.5	12.5

Table 7 Summary of Perforation Stability (Inclined Well, 180°/90° phasing, SPF 4)

Phasing [°]	180/90	180/90	180/90	180/90
Shot Density [SPF]	4	4	4	4
Depletion [psi]	-2980	-4200	-4500	-4500
Perforation Entrance Diameter [in]	0.2	0.2	0.2	0.2
Perforation Diameter at Middle [in]	0.5	0.5	0.5	0.5
Perforation Length [in]	10	10	10	10
Well Azimuth [°]	0	0	0	0
Well Inclination [°]	0	30	60	90
Perf Direction [°]	0	0	0	0

Phasing [°]	180/90	180/90	180/90	180/90
Shot Density [SPF]	4	4	4	4
Depletion [psi]	-2980	-2850	-2700	-3150
Perforation Entrance Diameter [in]	0.2	0.2	0.2	0.2
Perforation Diameter at Middle [in]	0.5	0.5	0.5	0.5
Perforation Length [in]	10	10	10	10
Well Azimuth [°]	0	0	0	0
Well Inclination [°]	0	30	60	90
Perf Direction [°]	0	90	90	90

The perforation has ellipsoidal-shaped geometry as shown in Figure 19. Failed Gauss point is shown as a colored point. In every case studied in the research, failed points (Gauss point) were observed at the cavity surface where;

- it is in the direction of least principal stress
- perforation tunnel diameter is large
- σ_H/σ_v is small

In other words, no failure was observed on the top & bottom (vertical well) and at the entrance & end of the perforation tunnel.

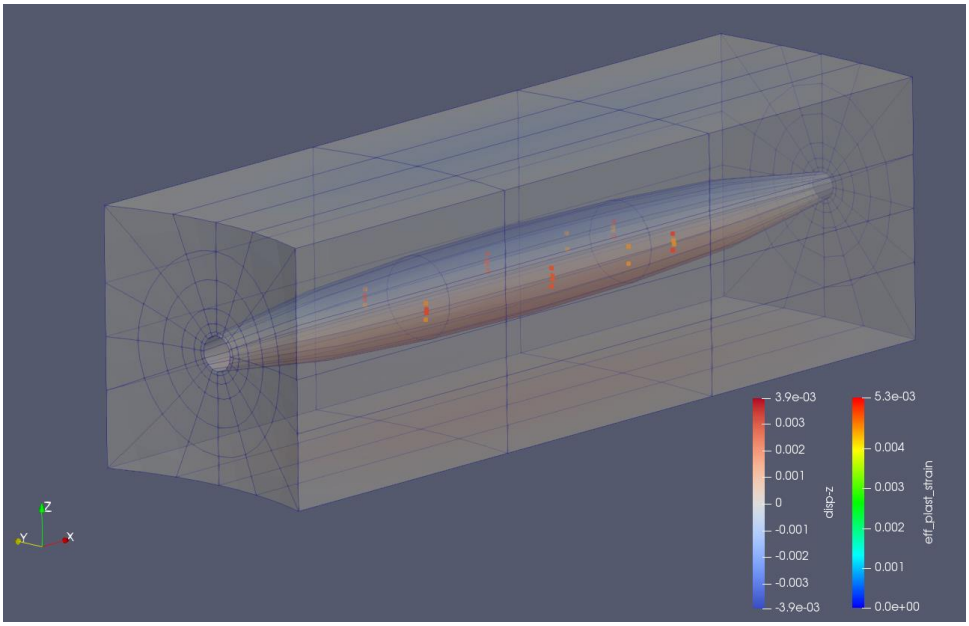

Figure 19 Example of Perforation Mesh with Failed Points (180°/90° phasing, SPF 8, Diameter 1.0”, Length 10”, In-situ Stress $\sigma_v^e : \sigma_H^e = 0.5 : 1.0$, Depletion 3,400 psi)

From field observation and current knowledge, it was expected that the strength of perforation would be higher with increasing shot density because of *release of vertical stress*. Release of vertical stress is explained below.

Assume there is only one cavity in the rock. Vertical stress and corresponding strain occur at the edge of the single perforation resulting in high stress concentration.

On the other hand, if there are more perforations as shown in Figure 20, stress and strain are distributed to every perforation resulting in less stress concentration. The “release of vertical stress” leads to the improvement of cavity stability with increasing shot density. However, the stability will be decreased with increasing shot density eventually since the radial stress becomes higher due to smaller area of solid part.

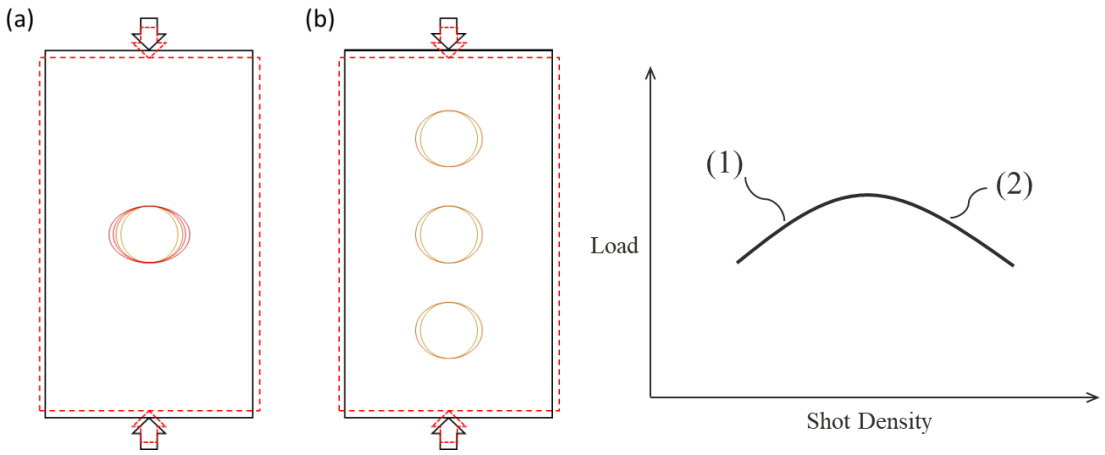

Figure 20 Schematic of Release of Vertical Stress

3.4.2.2 Effect of Shot Density and Phasing

Strength of perforation vs shot density (SPF) is plotted on Figure 21 for different perforation pattern; 120°/60° phasing (symmetry), 180°/90° phasing (symmetry), 180°/60° phasing (double spiral) and 90° phasing (single spiral). The 90° phasing (single

spiral) shows upward concave curve if shot density is from SPF 1 to SPF 4, which can be explained by release of vertical stress and increase of radial stress. However, the 90° phasing with very low shot density (SPF 0.5 – 1) and the other perforation patterns show downward concave curves, which was not expected. The positive-slope part of the curve is attributed to release of vertical stress, however, the negative-slope part should be resulted from other mechanism. The reason of the unexpected behavior is discussed in later section.

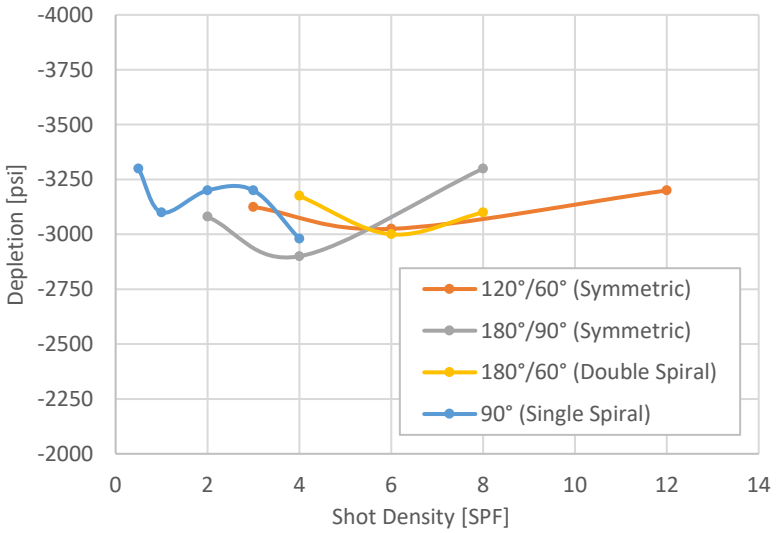

Figure 21 Effect of Perforation Pattern and Density on Perforation Stability

3.4.2.3 Effect of Perforation Diameter

For symmetry pattern such as 120°/60° phasing and 180°/90° phasing, perforation diameter has relatively small effect on perforation stability at small shot density (SPF 2 and 4 for 180°/90° phasing, SPF 3 and 6 for 120°/60° phasing). On the other hand, at higher shot density, perforation diameter has larger effect on perforation stability (Figure 22). The reason is that the effect of vertical stress release becomes larger as shot density increases (= vertical distance between perforations becomes smaller).

Note that, in a real field, large diameter perforation has higher possibility to contain a defect resulting in lower strength.

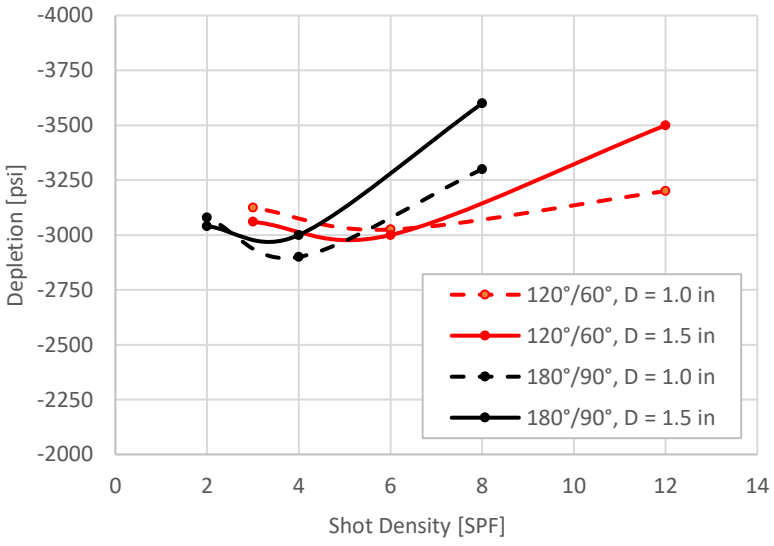

Figure 22 Effect of Perforation Diameter for Symmetric Pattern

For spiral pattern (180°/60° double spiral and 60° single spiral), the effect of perforation diameter is different from symmetric pattern (Figure 23). Although the positive slope is explained by release of vertical stress, the mechanism of the negative slope at low shot density is discussed in later section.

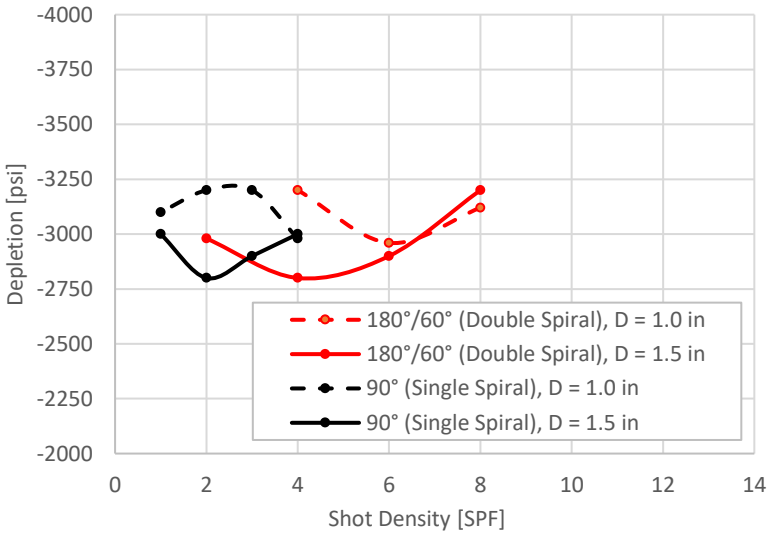

Figure 23 Effect of Perforation Diameter for Spiral Pattern

3.4.2.4 Effect of Perforation Length

Perforation is more stable if the length is longer (Figure 24). In the model, the curvature along perforation axis becomes gentle as the length becomes longer with constant diameter. This results in lower stress concentration on the cavity wall. In

addition, the most vulnerable point where perforation diameter is largest shifts outward resulting in lower stress concentration on the most vulnerable point.

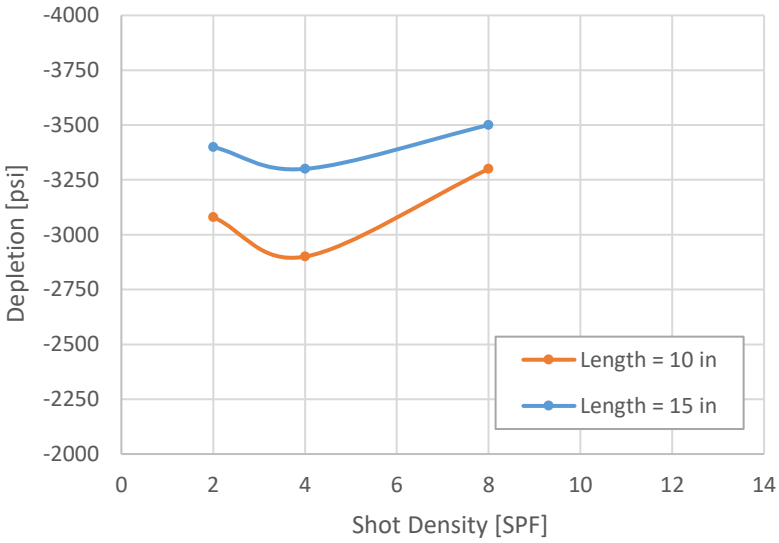

Figure 24 Effect of Perforation Length

3.4.2.5 Effect of Well Inclination

Although perforation stability in a vertical well has been evaluated in the preceding sections, inclined well is considered in this section. To account for relative positional relationship between a perforation and principal stresses, the well is inclined in two directions as shown in Figure 25.

In case (a), the perforation rotates downward/upward as the well is inclined. Perforation strength becomes significantly higher as the well inclination increases in this way (Figure 26). At 60° or higher inclination, any point on the perforation was not failed. It is thought that the improvement in strength with increasing well inclination is resulted from increasing σ_H/σ_v.

In case (b), the position and direction of the perforation remains the same for any inclination of the well. As the inclination is increased, the strength gradually reduces and then finally recovers to the original level (Figure 26). For this case (SPF 4), interaction between perforations are not significant, however, stress condition around casing becomes unbalanced due to the curvature of the cement-sand face when the well is slanted. Therefore, perforation strength becomes lower if the inclination is not 0° or 90°.

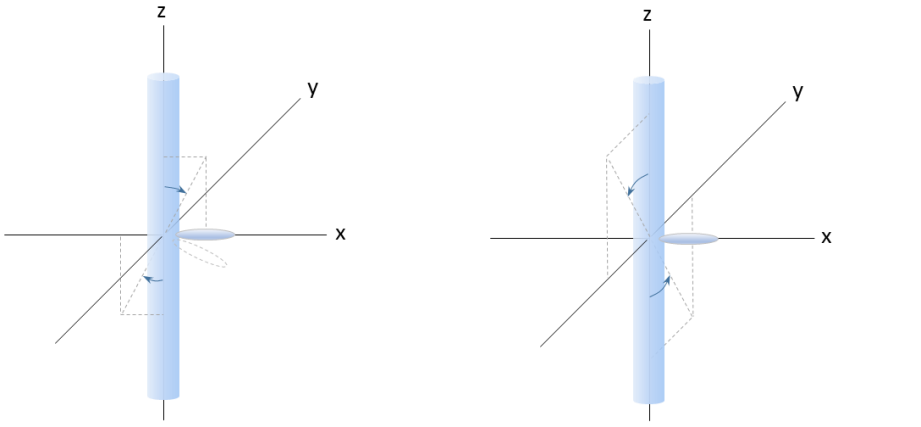

(a) Perforation rotates toward z-axis (b) Perforation remains parallel to x-axis

Figure 25 Schematic of Well Inclination

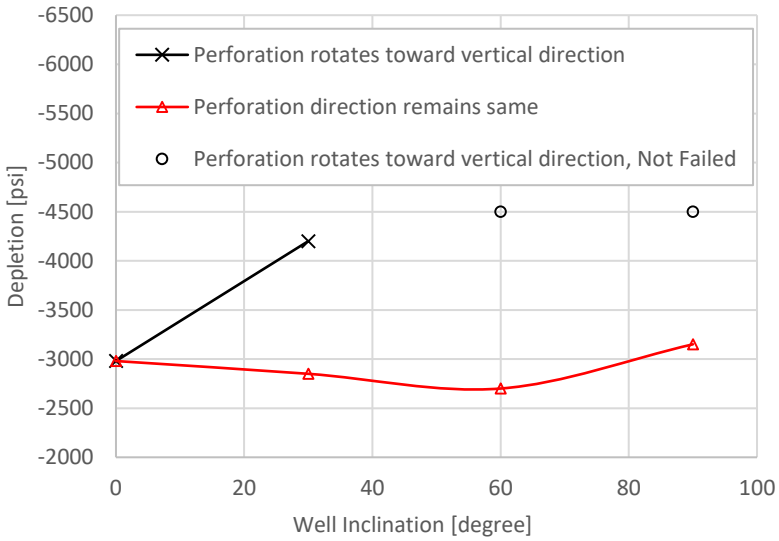

Figure 26 Effect of Well Inclination

3.4.2.6 Effect of In-situ Stress

In the preceding sections, the ratio of in-situ stress are assumed as $\sigma_x : \sigma_y : \sigma_v = -0.5 : -0.5 : -1.0$. In this section, perforation strength is evaluated as a function the stress ratio. Figure 27 shows the perforation strength for different in-situ stress ratios. Perforation is stable if the difference between σ_H ($= \sigma_x = \sigma_y$) and σ_v is small, and unstable if the difference is large. Also indicated is that the variation of in-situ stress ratio significantly affects the perforation stability.

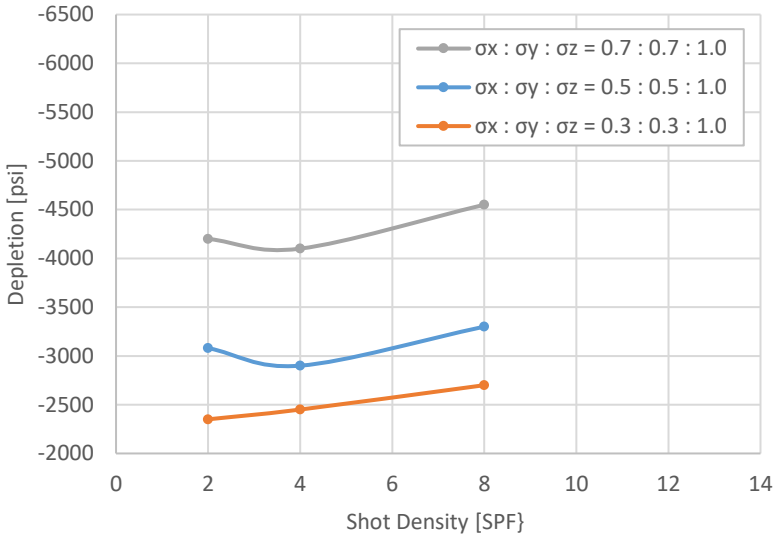

Figure 27 Effect of In-situ Stress Ratio

3.4.3 Discussion (Perforation Stability Evaluation)

3.4.3.1 Stress Change between Perforations

Release of vertical stress describes the mechanism how the perforation stability becomes better and eventually worse with increasing shot density. Now it is necessary why the stability becomes worse with increasing shot density at very low shot density.

First, it would be helpful to closely look at the vertical stress distribution. To see the interaction between perforations, the model is cut with a plane which crosses neighboring perforations (Figure 28). The distribution of vertical stress is plotted on the plane for 180°/90° phasing with SPF 2, SPF 4 and SPF 8 (Figure 29). In any of the three

cases, the stress state is captured at the same loading condition; 2,800 psi depletion (No failure occurred at this state). Note that the SPF 4 case is about to get failed at this moment since it got failed during next load increment (2,820 psi depletion).

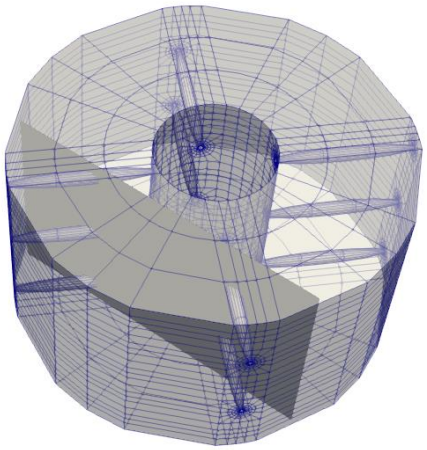

Figure 28 Plane Crossing the Neighboring Perforations

To see the extent of perforation interaction, the contour σ_z = -8.7 kpsi is drawn as white line (σ_z at a point where there is no interaction is -8.8kpsi). As shown in Figure 29, the contours are not connected each other in SPF 2 case indicating no or a little perforation interaction (no or little vertical stress release). On the other hand, the other two cases show a clear vertical interaction between perforations. If the effect of vertical stress release is dominant, SPF 4 case (which has a clear interaction) should shows higher perforation strength than SPF 2 case (which has no or a little interaction). However, SPF 4 has lower strength than SPF 2 case (Figure 21).

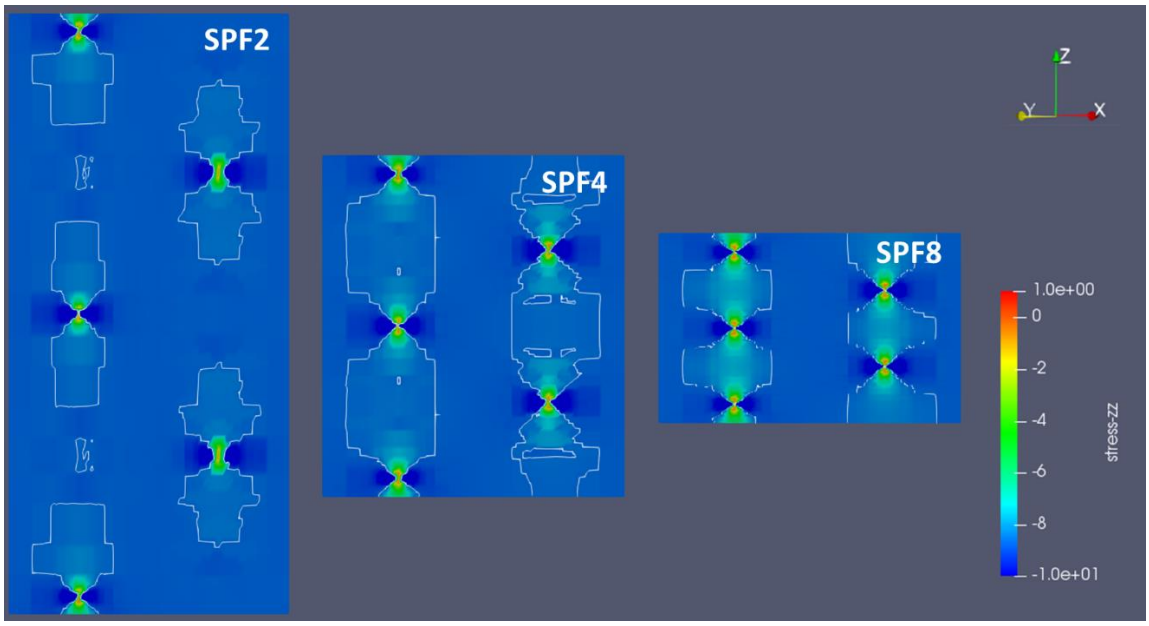

Figure 29 Distribution of Effective Vertical Stress (Contour: -8.7 kpsi)

From the fact that SPF 4 case shows lower stability despite of the clear vertical interaction, it is expected that the effect of vertical stress release is (partially) cancelled out by change of horizontal (tangential and radial) stresses. Tangential stress σ_θ and radial stress σ_r are obtained from the following equations and plotted on the plane (Figure 30 shows the distribution of σ_θ).

$$\sigma_\theta = \sigma_{xx}\, sin^2\,\theta + \sigma_{yy}\, cos^2\,\theta + 2\tau_{xy} sin\theta cos\theta$$

$$\sigma_r = \sigma_{xx}\, cos^2\,\theta + \sigma_{yy}\, sin^2\,\theta + 2\tau_{xy} sin\theta cos\theta$$

where $\theta = \arctan\left(\frac{y}{x}\right)$

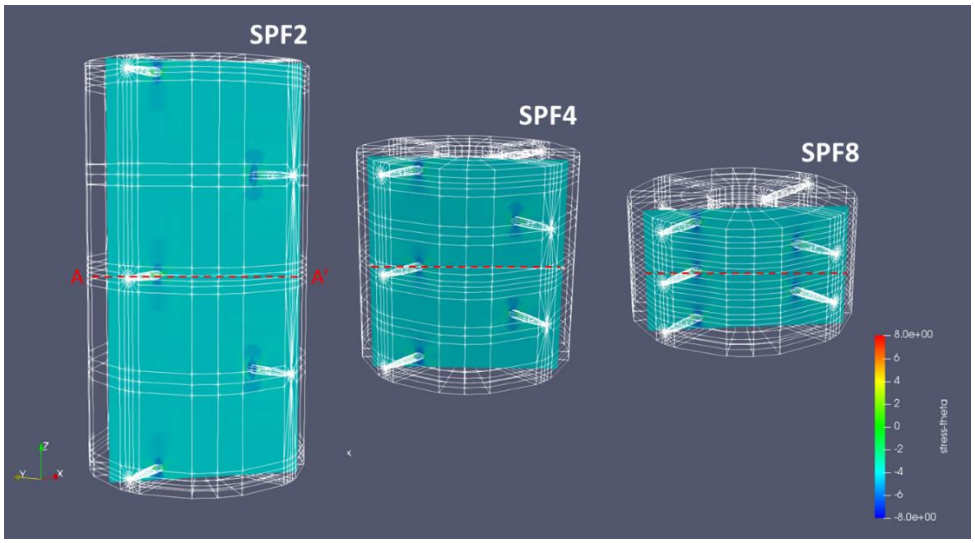

Figure 30 Distribution of Effective Tangential Stress

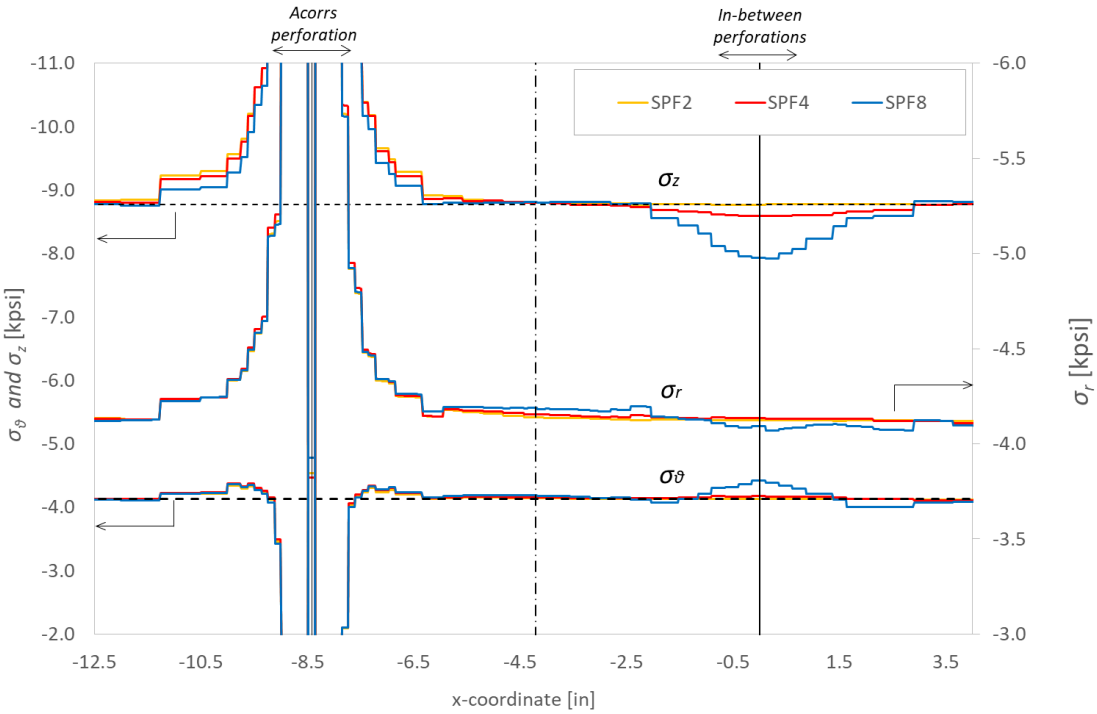

Figure 31 Profile of Effective Tangential Stress (Along A-A' in Figure 30)

Figure 31 is a profile of σ_θ along the line A-A' in Figure 30. From Figure 31, the interaction in-between perforations can be explained as below.

- In SPF 2 case, all the three stresses (σ_r, σ_θ and σ_z) do not change between the perforations.
- In SPF 4 case, σ_z is slightly reduced but σ_θ and σ_r are not changed between the perforations.
- In SPF 8 case, σ_z is reduced significantly but σ_θ is increased. σ_r is also decreased.

The observed fact indicates;

- Release of vertical stress takes place with the change of the other stress components (Poisson's effect)
- Magnitude of change in each stress component depends on shot density (= vertical and horizontal distance between perforations)
- In SPF 8 case, both decrease in σ_z and increase in σ_θ occurred. Therefore, the perforation of SPF 8 case became more stable than SPF 4 because the stress ratio $\sigma_z : \sigma_\theta$ was lowered.
- The reason why SPF 2 showed higher strength than SPF 4 case cannot be explained only by this result. This is to be discussed in next section.

3.4.3.2 Stress around Failed Point under the Effect of Perforation Interaction

Section 3.4.3.1 described the change of stresses between perforations. In this section, its effect on perforation surface around failing point is discussed. Figure 32 shows a plane which crosses the failed point at right angle to the perforation axis (= x-axis). The line B-B' on the plane is parallel to y-axis and crosses the perforation axis. Stress profile along the line B-B' is shown in Figure 33. On this plane or line, $\sigma_x \approx \sigma_r$ and $\sigma_y \approx \sigma_\theta$. Again, the stress state is captured at the moment when SPF 4 case is about to get failed. Thus, the stress state is almost equivalent to that of failure condition for SPF 4 case.

The results and interpretation of the stress profile are as below.

- SPF 2 has lowest σ_r, σ_θ, σ_z and τ_{oct} among all the three cases without release of vertical stress. The reason is that SPF 2 case has more solid part (less void space) than the others because of small shot density.
- SPF 4 shows highest σ_r, σ_θ, σ_z and τ_{oct} among all the three cases because; i) it has less solid part than SPF 2, and ii) it has less effect of vertical stress release than SPF 8.
- Despite of the least solid part among the three, stresses in SPF 8 case are just a little lower than SPF 4. This is attributed to the large effect of vertical stress release.

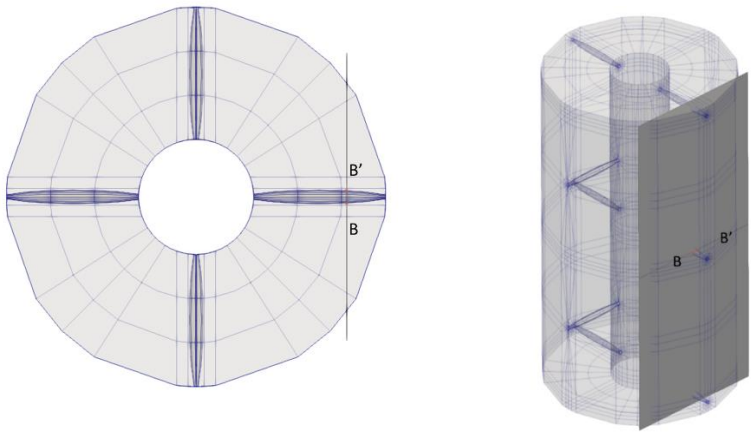

Figure 32 Plane across Perforation at Failed Point

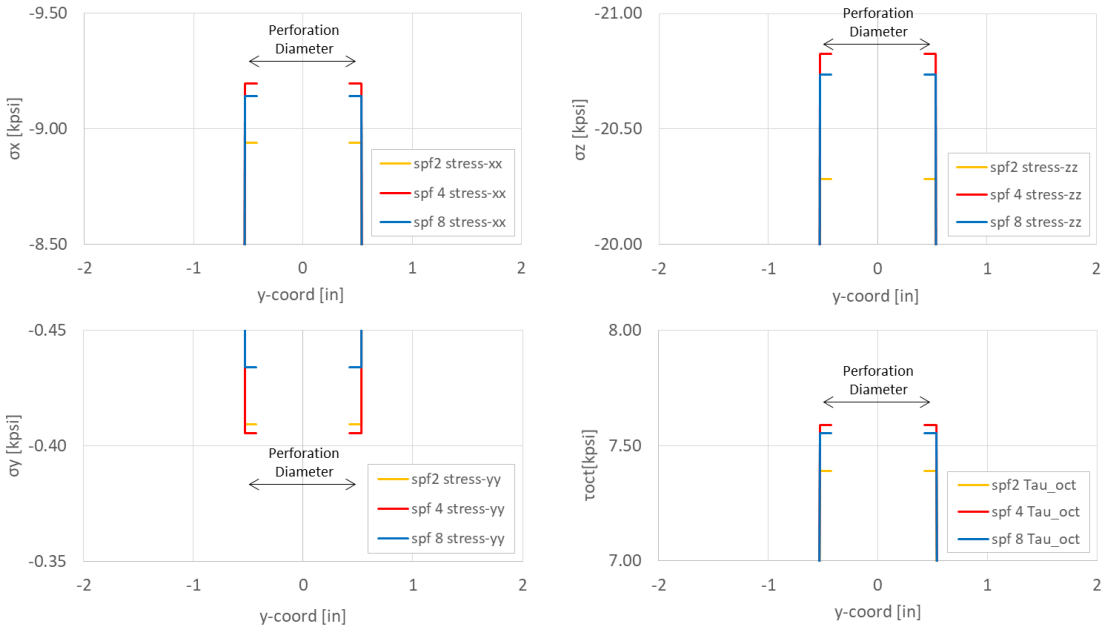

Figure 33 Stress Profile along the Line B-B'

3.4.3.3 Perforation Interaction as a Function of Shot Density

In Section 3.4.3.1 and 3.4.3.2, interaction in-between perforations and effect of interaction on perforation wall were discussed. By combining them and considering the release of vertical stress, following statement explains the perforation interaction as a function of shot density (Figure 34).

- Figure 34 (1) - (2)

  At very low shot density, there is not significant perforation interaction due to large distance between perforations. However, because of the slight interaction between diagonally located nearest perforations, the stress disturbance tends to be increased resulting in less stability of perforation. The perforation stability slightly reduces with a higher shot density if the shot density is small.

- Figure 34 (2) - (3)

  The effect of vertical stress release becomes dominant as the perforations get closer each other. Perforation stability is improved by increasing shot density.

- Figure 34 (3) - (4)

  With much higher shot density, radial stress becomes higher due to too much void.

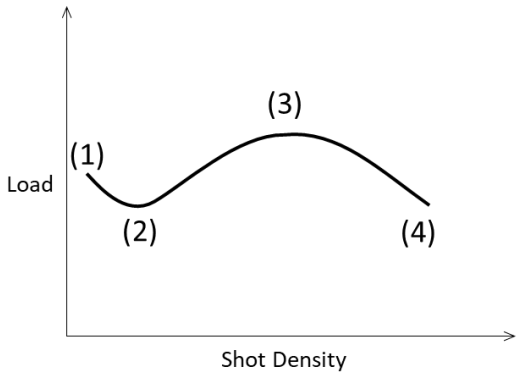

Figure 34 Schematic of Perforation Stability as a Function of Shot Density

3.4.3.4 Perforation Interaction in Spiral Pattern

Considering the above mentioned mechanism, spiral pattern (180°/60° double spiral and 90° single spiral) is examined again here. As shown in Figure 4, in spiral pattern, vertical distance is larger and diagonal/horizontal distance is smaller than symmetric pattern when compared at same shot density. Therefore, increase in perforation diameter has less effect on vertical stress release but does have impact on tangential stress release. Therefore, perforation is stronger with 1.0” diameter and weaker with 1.5” diameter.

3.4.3.5. Effect of Perforation Length on Interaction

Vertical distance between perforations remains the same for any perforation length but horizontal distance becomes larger according to perforation length (Figure 35). Hence, the stress interaction in vertical direction remains the same for longer perforations. On the other hand, the stress disturbance around the cemented sand-face is

reduced. It means that the farther from perforation wall is, the more stable the point is. Therefore, increasing the length of perforation does not make the perforation unstable.

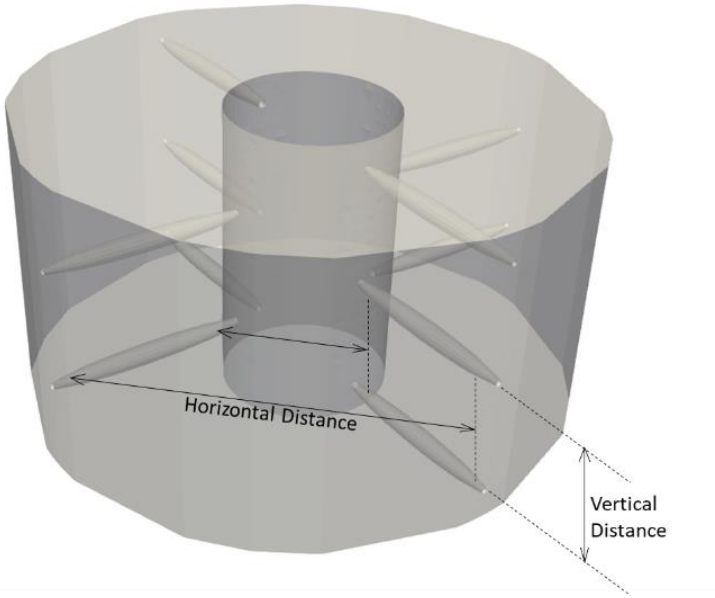

Figure 35 Schematic of Perforations

3.5 Recommendation

1) As for flow performance, it was shown that a higher shot density yields higher productivity. However, if shot density is limited to low and/or vertical permeability is low, perforation pattern must be chosen carefully because the pattern affects the productivity significantly.

2) Although change in perforation diameter has small impact on productivity, longer perforation shows apparently better flow performance. Thus, longer perforation is more prolific.
3) Sand production may enhance productivity by enlarging the cavity diameter and removing perforating damage zone. One should quantitate the improvement of production and also additional cost to allow sand production.
4) Among the cases studied in this research, if the perforation diameter is 1.0" and length is 10", 180°/90° phasing with SPF 8 has the highest strength. The perforation pattern becomes more stable with larger diameter (1.5") and longer length (15").
5) Perforation stability is sensitive to perforation diameter. The sensitiveness implies the importance of re-meshing in sand rate prediction model.
6) Because in-situ stress ratio (horizontal/vertical in-situ stress) has the largest impact on perforation stability, it should be obtained with a good accuracy.

4. CONCLUSIONS

The multi-perforation numerical models using the finite element method were developed for flow simulation and geomechanics simulation. They provided quantitative evaluation results of perforation flow performance and perforation mechanical stability.

The investigation of interaction between perforations revealed perforation stability as a function of shot density. The relation between stability and shot density can be decomposed into three stages.

- At very low shot density (Figure 34 (1)-(2)), there is no perforation interaction. Perforation stability slightly decreases with increasing shot density because of the stress disturbance between the nearest diagonal perforations. There is little effect of vertical stress release.
- With higher density (Figure 34 (2)-(3)), perforation stability is improved by increasing shot density. The effect of vertical stress release is dominant.
- With too high shot density (Figure 34 (3)-(4)), perforation becomes unstable due to high radial stress.

Overall, perforation stability is affected by vertical stress reduction, tangential stress reduction and the disturbance from the curved cement-sand face.

REFERENCES

Ahrens, J., Geveci, Berk, Law, Charles. (2005). ParaView: An End-User Tool for Large Data Visualization. *Visualization Handbook*(Elsevier).

Arii, H., Morita, N., Ito, Y., & Takano, E. (2005). *Sand-Arch Strength Under Fluid Flow With and Without Capillary Pressure*. Paper presented at the SPE Annual Technical Conference and Exhibition, Dallas, Texas.

E. Fjaer, R. M. H., P. Horsrud, A. M. Raaen and R. Risnes. (2008). Petroleum Related Rock mechanics 2nd Edition. (Elsevier).

Fuh, G.-F., & Morita, N. (2013). *Sand Production Prediction Analysis of Heterogeneous Reservoirs for Sand Control and Optimal Well Completion Design*. Paper presented at the International Petroleum Technology Conference, Beijing, China.

Hinton, D. R. J. O. a. E. (1980). Finite Elements in Plasticity: Theory and Practice. (Pineridge Press Limited).

Karakas, M., & Tariq, S. M. (1991). Semianalytical Productivity Models for Perforated Completions. doi:10.2118/18247-PA

Liou, J. (2014). Keeping sand at bay.

Papamichos, E., Stenebraten, J., Cerasi, P., Lavrov, A., Vardoulakis, I., Fuh, G. F., . . . Havmoller, O. (2008). *Rock type and hole failure pattern effects on sand production*. Paper presented at the The 42nd U.S. Rock Mechanics Symposium (USRMS), San Francisco, California.

W.T. Bell, R. A. S., S.M. Tariq. (1995). Perforating. *Monograph Volume 16*(SPE).

Wang, H., & Sharma, M. M. (2017). *The Role of Elasto-Plasticity in Cavity Shape and Sand Production in Oil and Gas Wells*. Paper presented at the SPE Annual Technical Conference and Exhibition, San Antonio, Texas, USA.

Yacob Fish, T. B. (2007). A First Course in Finite Elements. (Wiley).

Zoback, M. D. (2007). Reservoir Geomechanics. (Cambridge).

APPENDIX

ERROR ESTIMATION OF STRESS STATE AROUND AN INCLINED WELL

The current model uses very course mesh with only six divisions in the radial direction. Analytical solution available for similar problems is the stress state around an inclined well with a given well pressure as shown in the figure. Although the perforation problems and borehole problems have different boundary conditions, the error estimation using the analytical solution for inclined wells are used in this section since the mesh is common around a borehole except for perforations.

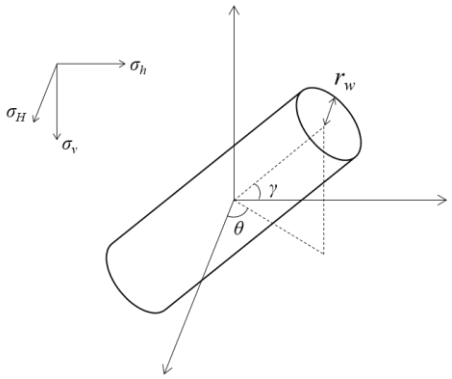

Figure A-1 Schematic of an Inclined Well

Suppose the in-situ stresses are given by $(\sigma_H, \sigma_h, \sigma_V)$ in (x', y', z') coordinate. The azimuth and inclination of an inclined well is given by (θ_1, γ) where the coordinate of the inclined well is (x, y, z). The stress in the well coordinate is given by $\sigma_x, \sigma_y, \sigma_z,$ $\tau_{yz}, \tau_{zx}, \tau_{xy}$, where

$$\sigma_x = \ell_1^2\sigma_H + m_1^2\sigma_h + n_1^2\sigma_V$$

$$\sigma_y = \ell_2^2\sigma_H + m_2^2\sigma_h + n_2^2\sigma_V$$

$$\sigma_z = \ell_3^2\sigma_H + m_3^2\sigma_h + n_3^2\sigma_V$$

$$\tau_{yz} = \ell_2\ell_3\sigma_H + m_2m_3\sigma_h + n_2n_3\sigma_V$$

$$\tau_{zx} = \ell_3\ell_1\sigma_H + m_3m_1\sigma_h + n_3n_1\sigma_V$$

$$\tau_{xy} = \ell_1\ell_2\sigma_H + m_1m_2\sigma_h + n_1n_2\sigma_V$$

Directional cosines are given in Table A-1.

Table A-1 Directional Cosines

	x'	y'	z'
x	$l_1 = cos\theta_1 cos\gamma$	$m_1 = cos\gamma sin\theta_1$	$n_1 = -sin\gamma$
y	$l_2 = -sin\theta_1$	$m_2 = cos\theta_1$	$n_2 = 0$
z	$l_3 = cos\theta_1 sin\gamma$	$m_3 = sin\theta_1 sin\gamma$	$n_3 = cos\gamma$

Using $\sigma_x, \sigma_y, \sigma_z, \tau_{yz}, \tau_{zx}, \tau_{xy}$, the stress around the inclined well is given by

$$\sigma_r = 0.5(\sigma_x + \sigma_y)(1 - r_d^{-2}) + 0.5(\sigma_x - \sigma_y)(1 - 4r_d^{-2} + 3r_d^{-4})cos2\theta + \tau_{xy}(1 - 4r_d^{-2} + 3r_d^{-4})sin2\theta - P_w r_d^{-2} - \frac{E}{1+\nu}\beta r^{-2}\int_{r_w}^{r} r\Delta p dr$$

$$\sigma_\theta = 0.5(\sigma_x + \sigma_y)(1 + r_d^{-2}) - 0.5(\sigma_x - \sigma_y)(1 + 3r_d^{-4})cos2\theta + \tau_{xy}(1 + 3r_d^{-4})sin2\theta + P_w r_d^{-2} + \frac{E}{1+\nu}\beta r^{-2}\int_{r_w}^{r} r\Delta p dr - \frac{E}{1-\nu}\left(\frac{1}{3B} - \frac{1}{3B_i}\right)\Delta p$$

where

$$\frac{1}{3B} = \frac{1-2\nu}{E}$$

$$\frac{1}{3B_i} = \frac{1-2\nu_i}{E_i}$$

$$r_d = \frac{r}{r_w}$$

$$\sigma_z = \sigma_{zz} - \nu\left[2(\sigma_x - \sigma_y)r_d^{-2}cos2\theta + 4\tau_{xy}r_d^{-2}sin2\theta\right] - \frac{E}{1-\nu}\left(\frac{1}{3B} - \frac{1}{3B_i}\right)\Delta p$$

$$\tau_{r\theta} = 0.5(\sigma_x - \sigma_y)(-1 - 2r_d^{-2} + 3r_d^{-4})sin2\theta + \tau_{xy}(1 + 2r_d^{-2} - 3r_d^{-4})cos2\theta$$

$$\tau_{\theta z} = (1 + r_d^{-2})(-\tau_{xz}sin\theta + \tau_{yz}cos\theta)$$

$$\tau_{rz} = (1 - r_d^{-2})(\tau_{xz}cos\theta + \tau_{yz}sin\theta)$$

$$u = 0.5\sigma_x r_w \frac{1+\nu}{E}\left((1-2\nu)r_d + r_d^{-1}\right) + r_w P_w \frac{1+\nu}{E} r_d^{-1}$$
$$+ \left(\sigma_x - \sigma_y\right) r_w \frac{1+\nu}{E\nu}\left(0.5 r_d - 0.5 r_d^{-3} + \frac{2\nu}{1+\nu} r_d^{-1}\right) cos2\theta$$
$$+ 0.5\sigma_y r_w \frac{1+\nu}{E}\left((1-2\nu)r_d + r_d^{-1}\right)$$
$$- \tau_{xy} r_w \frac{1+\nu}{E\nu}\left(-r_d + r_d^{-3} - 4\frac{\nu}{1+\nu} r_d^{-1}\right) sin2\theta$$
$$+ \frac{1+\nu}{E}\tau_{xz} z cos\theta + \frac{1+\nu}{E}\tau_{yz} z sin\theta + \beta r^{-1}\int_{r_w}^{r} r\Delta p dr$$

$$v = \left(\sigma_x - \sigma_y\right) r_w \frac{1+\nu}{E\nu} x \left\{-0.25(1+\nu)r_d + 0.25(1-3\nu)r_d^{-3}\right.$$
$$\left. - \frac{\nu(1-\nu)}{1+\nu} r_d^{-1}\right\} cos2\theta$$
$$+ \tau_{xy} r_w \frac{1+\nu}{E\nu} x \left\{0.5(1+\nu)r_w - 0.5(1-3\nu)r_d^{-3}\right.$$
$$\left. - \frac{2\nu(1-\nu)}{1+\nu} r_d^{-1}\right\} cos2\theta - \frac{1+\nu}{E}\tau_{xz} z sin\theta + \frac{1+\nu}{E}\tau_{yz} z cos\theta$$

$$w = \frac{1+\nu}{E}\tau_{xz} r_w \left(r_d + \frac{2}{r_d}\right) cos\theta + \frac{1+\nu}{E}\tau_{yz} r_w \left(r_d + \frac{2}{r_d}\right) sin\theta$$

The above displacement includes the displacement induced by the in-situ stress. The displacement induced after drilling the well is given as follows.

$$u' = 0.5\sigma_x r_w \frac{1+\nu}{E} r_d^{-1} + r_w P_w \frac{1+\nu}{E} r_d^{-1}$$
$$+ (\sigma_x - \sigma_y) r_w \frac{1+\nu}{E\nu} \left(-0.5 r_d^{-3} + \frac{2\nu}{1+\nu} r_d^{-1}\right) cos2\theta$$
$$+ 0.5\sigma_y r_w \frac{1+\nu}{E} r_d^{-1} - \tau_{xy} r_w \frac{1+\nu}{E\nu} \left(r_d^{-3} - \frac{4\nu}{1+\nu} r_d^{-1}\right) sin2\theta$$
$$+ \beta r^{-1} \int_{r_w}^{r} r \Delta p dr$$

$$v' = (\sigma_x - \sigma_y) r_w \frac{1+\nu}{E\nu} x \left\{0.25(1-3\nu) r_d^{-3} - \frac{\nu(1-\nu)}{(1+\nu) r_d^{-1}}\right\} cos2\theta$$
$$+ \tau_{xy} r_w \frac{1+\nu}{E\nu} x \left\{-0.5(1-3\nu) r_d^{-3} - \frac{2\nu(1-\nu)}{1+\nu} r_d^{-1}\right\} cos2\theta$$

$$w' = \frac{1+\nu}{E} \tau_{xz} r_w \frac{2}{r_d} cos\theta + \frac{1+\nu}{E} \tau_{yz} r_w \frac{2}{r_d} \sin\theta$$

Figure A-2 is a mesh which is used to obtain numerical solution to be compared with analytical solution. The mesh represents a wellbore without perforation and is same as a mesh for 120°/60° phasing pattern except for the absence of perforation. The three elements shown in Figure A-3 correspond to a location where perforation may exist. Stresses are evaluated at Gauss points in the elements (5th Gauss points in element 2357, 2373 and 2389. Figure A-3). Assume that perforation length is 9.75" and well radius is 4.25". Then, *r* and r_d of the 5th Gauss points are obtained as;

$r = 4.25 + 3.25 \times 1/2 = 5.875$ then $r_d = r/r_w = 1.382$

$r = 4.25 + 3.25 \times 3/2 = 9.125$ then $r_d = r/r_w = 2.147$

$r = 4.25 + 3.25 \times 5/2 = 12.375$ then $r_d = r/r_w = 2.911$

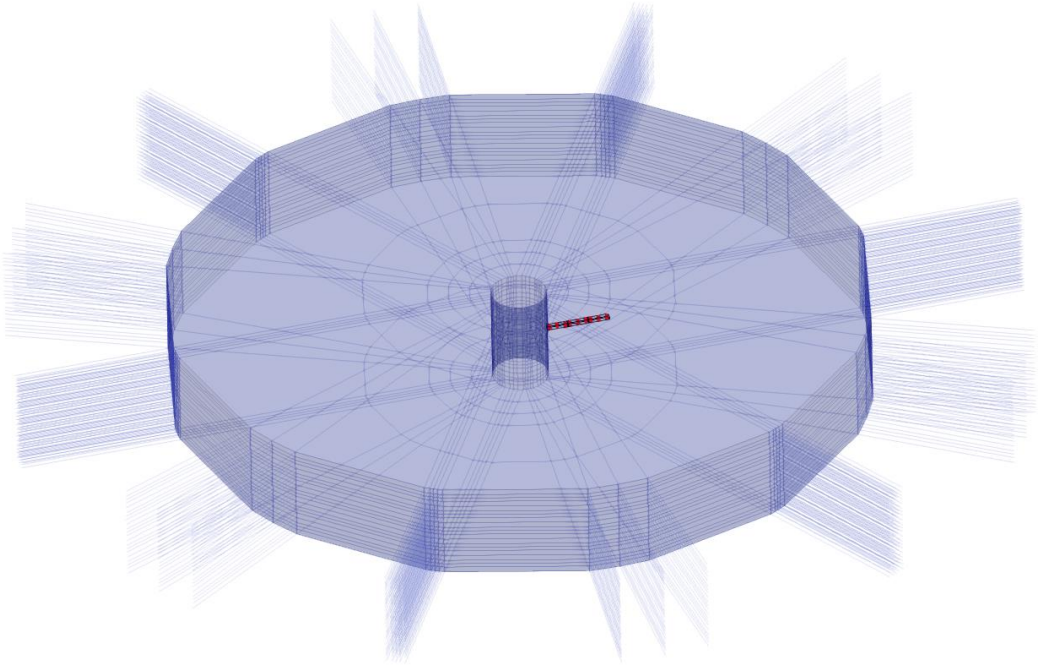

Figure A-2 Mesh of Wellbore Model

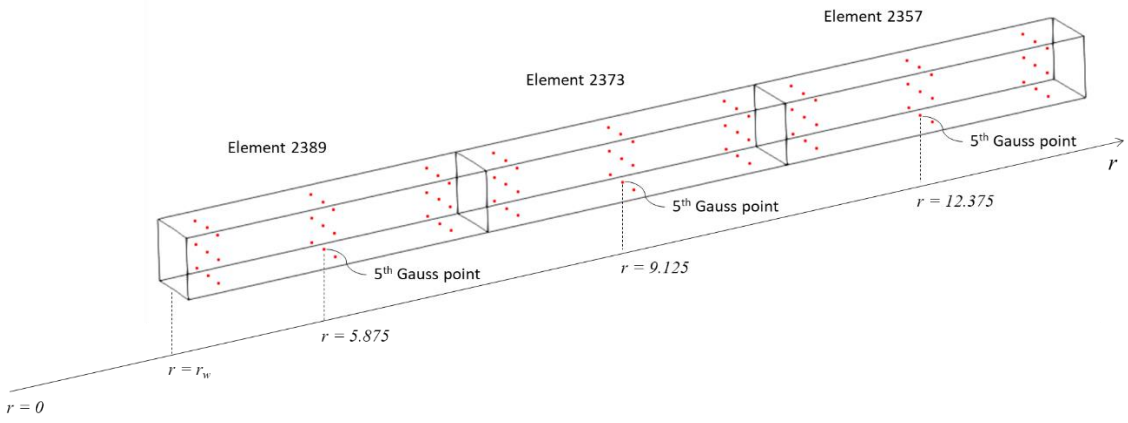

Figure A-3 Elements and Gauss Points for Error Check

All the stresses are net stresses where the initial pore pressure is subtracted. In-situ stresses are σ_H= -3kpsi, σ_h = -3kpsi and σ_v= -6kpsi. Tables A-2 to A-5 compare the analytical results and numerical results with the same mesh around a well as used for the perforation stability analysis. The difference of the stress state is within 200 psi for $r_d = 2.147$ and $r_d = 2.911$ where the perforation failure normally induced. The stress state near the well has 450 psi maximum error. The error becomes higher near well since the mesh is coarse in the radial direction. However, since no instability of perforation is observed at the location adjacent to the well, the inaccuracy of the stress state at the perforation inlet may be ignored.

Table A-2 Comparison of the principal stresses around an openhole at r/r_w = 1.382, 2.147 and 2.911, where the perforation meshes are located (well inclination 0°). Unit for pressure and stress is kpsi.

p_p	r_d	Numerical Solution			Analytical Solution		
		σ_r	σ_θ	σ_z	σ_r	σ_θ	σ_z
1.00	1.38	-1.84	-4.00	-6.00	-1.95	-4.05	-6.00
1.00	2.14	-2.55	-3.43	-6.00	-2.56	-3.43	-6.00
1.00	2.91	-2.76	-3.23	-6.00	-2.76	-3.24	-6.00
0.00	1.38	-1.26	-4.50	-5.94	-1.43	-4.57	-6.00
0.00	2.14	-2.32	-3.64	-5.99	-2.35	-3.65	-6.00
0.00	2.91	-2.64	-3.35	-5.99	-2.65	-3.35	-6.00

Table A-3 Comparison of the principal stresses around an openhole at r/r_w = 1.382, 2.147 and 2.911, where the perforation meshes are located (well inclination 30°). Unit for pressure and stress is kpsi.

p_p	r_d	Numerical Solution			Analytical Solution		
		σ_r	σ_θ	σ_z	σ_r	σ_θ	σ_z
1.00	1.38	-1.47	-3.91	-5.50	-1.91	-3.94	-5.21
1.00	2.14	-2.34	-3.45	-5.75	-2.56	-3.46	-5.58
1.00	2.91	-2.64	-3.26	-5.86	-2.77	-3.26	-5.75
0.00	1.38	-0.94	-4.41	-5.41	-1.41	-4.46	-5.19
0.00	2.14	-2.14	-3.67	-5.71	-2.38	-3.68	-5.55
0.00	2.91	-2.54	-3.37	-5.83	-2.67	-3.38	-5.73

Table A-4 Comparison of the principal stresses around an openhole at r/r_w = 1.382, 2.147 and 2.911, where the perforation meshes are located (well inclination 60°). Unit for pressure and stress is kpsi.

p_p	r_d	Numerical Solution			Analytical Solution		
		σ_r	σ_θ	σ_z	σ_r	σ_θ	σ_z
1.00	1.38	-3.71	-4.11	-1.30	-3.56	-3.71	-1.90
1.00	2.14	-4.82	-3.50	-2.30	-4.67	-3.52	-2.63
1.00	2.91	-5.36	-3.31	-2.64	-5.22	-3.32	-2.81
0.00	1.38	-4.04	-4.41	-1.66	-3.49	-4.23	-1.45
0.00	2.14	-4.80	-3.71	-2.19	-4.56	-3.74	-2.53
0.00	2.91	-5.30	-3.42	-2.59	-5.15	-3.44	-2.77

Table A-5 Comparison of the principal stresses around an openhole at r/r_w = 1.382, 2.147 and 2.911, where the perforation meshes are located (well inclination 90°). Unit for pressure and stress is kpsi.

p_p	r_d	Numerical Solution			Analytical Solution		
		σ_r	σ_θ	σ_z	σ_r	σ_θ	σ_z
1.00	1.38	-2.22	-3.69	-2.33	-2.26	-3.60	-2.37
1.00	2.14	-4.15	-3.51	-2.65	-4.15	-3.55	-2.74
1.00	2.91	-4.94	-3.34	-2.81	-4.94	-3.35	-2.86
0.00	1.38	-1.74	-4.18	-2.19	-1.74	-4.12	-2.37
0.00	2.14	-3.97	-3.67	-2.64	-3.93	-3.76	-2.74
0.00	2.91	-4.82	-3.45	-2.81	-4.82	-3.47	-2.86